March 27th 2015

Equation of state and elasticity of the 3.65 Å phase- implications for the X-discontinuity

Mainak Mookherjee[1*], Sergio Speziale[2#], Hauke Marquardt[2+], Sandro Jahn[2], Bernd Wunder[2], Monika Koch-Müller[2], Hanns-Peter Liermann[3]

[1]Earth and Atmospheric Sciences, Cornell University, Ithaca, NY 14853, USA.

[*]mainak.mookherjee@cornell.edu

[2]Deutsches GeoForschungsZentrum GFZ, Section 3.3, Telegrafenberg, 14473, Potsdam, Germany.

[#]speziale@gfz-potsdam.de

[+]now at: Bayerisches Geoinstitut, University of Bayreuth, 95440 Bayreuth, Germany.

[3]Deutsches Elektronen Synchrotron, DESY, Hamburg, Germany.

Abstract

The 3.65 Å phase [$MgSi(OH)_6$] is likely to be formed by decomposition of the hydrous 10 Å phase [$Mg_3Si_4O_{10}(OH)_2.H_2O$] at pressures of 9-10 GPa. In this study, we use a combination of X-ray diffraction and *first principles* simulations to constrain the equation of state and elasticity of the 3.65 Å phase. We find that the equation-of-state results for the 3.65 Å phase, from X-ray diffraction data are well represented by a third order Birch-Murnaghan formulation, with K_0 = 83.0 (± 1.0) GPa, K_0' = 4.9 (± 0.1) and V_0 = 194.52 (± 0.02) Å^3. Based on the *first principles* simulations, the full single crystal elastic constant tensor with monoclinic symmetry shows significant anisotropy with the compressional

components- c_{11} = 156.2 GPa, c_{22} = 169.4 GPa, c_{33} = 189.3 GPa, the shear components c_{44} = 55.9 GPa, c_{55} = 58.5 GPa, c_{66} = 74.8 GPa, and c_{46} = 1.6 GPa; the off diagonal components c_{12} = 38.0 GPa, c_{13} = 26.5 GPa, c_{23} = 22.9 GPa, c_{15} = 1.5 GPa, c_{25} = 1.5 GPa, and c_{35} = -1.9 GPa at zero pressure.

At depths corresponding to 270-330 km, seismological X- discontinuity has been observed in certain regions. We find that the formation of 3.65 Å from layered hydrous magnesium silicates (LHMS) such as 10 Å angstrom phases occurs at around 9 GPa i.e., coinciding with the seismic X-discontinuity. The LHMS phases have significant seismic anisotropy. Based on the full elastic constant tensor, although among the dense hydrous magnesium silicate (DHMS) phases, the 3.65 Å phase reveals considerably larger elastic anisotropy, it is significantly smaller than the LHMS phases. This change in seismic anisotropy in hydrous phases might be one of the plausible explanations for the seismic X-discontinuity.

Key Words: 3.65 Å phase, X-discontinuity, Mantle hydration, Elasticity, Equation of state, High-Pressure

1. Introduction

Hydrous phases play an important role in transporting water into the Earth's interior. At crustal and shallower depths, layered hydrous silicates, such as serpentine, talc, chlorite, muscovite, and phlogopite are predominant. However at greater depths these hydrous phases become thermodynamically unstable and they dehydrate and part of the released fluid migrates up to the arc

thus affecting the surrounding mantle. These fluids dictate the onset of hydrous melting (Iwamori, 1998, 2007, Kawamoto, 2006, Frost, 2006) and may trigger deep earthquakes (Brudzinski et al., 2007). Mantle hydration has also been invoked to explain various geophysical observations including the '*inverted moho*' in the mantle wedges (Bostock et al., 2002, Bezacier et al., 2010, 2013, Mookherjee and Capitani, 2011), 'low velocity layers' in subducting lithosphere (Abers, 2005, Chantel et al., 2012, Mookherjee and Bezacier, 2012, Kim et al., 2012, 2013). In addition, unusually large delay times between the arrivals of the two shear waves have also been explained by presence of hydrous phases in certain subduction zone settings (Long and Silver, 2008, Katayama et al., 2009, Bezacier et al., 2010, Jung et al., 2011, Mookherjee and Capitani, 2011).

However, dehydration is almost certainly incomplete and the remaining fluid is partitioned into the dense hydrous magnesium silicate phase (DHMS). A number of dense hydrous magnesium silicate phases have been identified based on experiments conducted in the simplified three-component system, MgO-SiO_2-H_2O which is representative of hydrated peridotite lithology (Ringwood and Major, 1967, Gasparik, 1993, Prewitt and Downs, 1998, Angel, 2001, Clark et al., 2004; Gleason et al., 2008). The 3.65 Å phase $MgSi(OH)_6$ is one such DHMS phase that has been known for a while (Sclar, 1965). However, its crystal structure and phase stability remained poorly understood until recent studies (Pawley et al., 2011, Welch and Wunder, 2012; Wunder et al., 2011, 2012). Based on these experiments, at pressures of 9-10 GPa, the hydrous 3.65 Å phase ($MgSi(OH)_6$) is likely to be formed as breakdown product of the 10 Å phase ($Mg_3Si_4O_{10}(OH)_2.H_2O$) (Pawley et al., 2011, Wunder et al., 2011, 2012). It is

capable of hosting significant amount of water ~ 35 wt%, and is one of the largest repositories of water among all the known hydrous phases.

The 3.65 Å phase is a hydroxide perovskite. A typical perovskite mineral phase has ABO_3 stoichiometry with corner sharing BO_6 octahedral units forming a framework and a twelve fold coordinated A site. In the 3.65 Å phase the A site is empty and the magnesium and silicon atoms occupy the octahedral units that form the charge neutral framework, with hydroxyl groups forming hydrogen bonds (Kleppe et al., 2012) (**Fig. 1**). The 3.65 Å phase has a primitive unit-cell with a space group $P2_1$ with 28 atoms in the unit cell (Z=2) (Wunder et al., 2012).

Despite being one of the largest repositories of water among all the known hydrous phases, its physical properties remain poorly understood. In this study, we explore the equation of state and elasticity of 3.65 Å phase at high pressures using synchrotron X-ray diffraction and complementary first principle simulations.

2. Methods

2. 1. Synthesis & High pressure X-ray diffraction

The sample material used in this study is a fraction of that investigated in three previous studies (Wunder et al., 2011, 2012; Welch and Wunder, 2012) The synthesis was performed at 425 ^{0}C and 10 GPa for 77 hrs in the 800 ton rotating multi-anvil press apparatus installed at the GeoForschungsZentrum GFZ, Potsdam, Germany (Wunder et al., 2011). The electron probe microanalysis of around forty-three crystals of 3.65 Å phase yielded a mean Mg/Si rato of 1.02 (±0.06) and the MgO and SiO_2 oxide mean analytical sum was 66.5 (±3.2) (Wunder et al. 2011). The water content of 3.65 Å phase was determined by

integrating the area (A_{OH}) under hydroxyl stretching frequency region (2800-3800 cm^{-1}) from infrared spectroscopy (Wunder et al., 2011). Beer-Lambert law ($c_{H_2O} = 1.8 \times \varepsilon A_{OH} \rho t$) with integrated molar absorption coefficient (ε) from linear calibration of nominally anhydrous minerals, hydrous minerals, and hydrous glasses (Libowitzky and Rossman, 1997) yielded c_{H_2O} = 34.0 (±3.0) wt% (Wunder et al., 2011). The symbols (ρ) and (t) refer to the density and thickness of sample of 3.65 Å phase. The details of the chemical analysis are reported in two earlier studies (Wunder et al., 2011, 2012).

The sample was disaggregated and ground to a powder with particle-size less than 5 μm. Three powder batches were compressed between 300 μm size diamond culets using symmetric diamond anvil cells (Mao and Bell, 1980). The samples were loaded in 150 μm diameter sample chambers drilled in rhenium (Re) foils of 250 μm initial thickness, pre-indented to 30 to 40 μm. One or two ruby spheres were placed close to the rim of the sample chambers and used as a pressure calibrant (Mao et al., 1986). In one experiment (experiment 1, see Table 1) a small fragment of a 5 μm thick Au foil was also loaded as a pressure calibrant. Ne was used as a pressure-transmitting medium. It was loaded at a pressure of 1500 to 1900 bars either at the gas loading facility at the GFZ or at that available at the Extreme Conditions Beamline (ECB) of PETRA III synchrotron source at HASYLAB, Hamburg.

Angle-dispersive X-ray diffraction measurements were performed at high pressures and ambient temperature at the ECB P02.2 of PETRA III (**Table 1**). The energy of the monochromatic X-ray beam was 42.8 keV (corresponding to a wavelength of 0.2897 Å) in experiment 1, 42.7 keV (0.2904 Å) in experiment 2

and 42.4 keV (0.2922 Å) in experiment 3. Additional details of the experimental setup available at beamline P02.2 are reported elsewhere (Liermannn et al., 2010). The diamond facing the X-ray detector was supported by a plate of cubic BN that is partially transparent to the X-ray radiation used in these experiments providing access to a larger range of reciprocal space. The X-ray diffraction images were collected with Perkin-Elmer XRD-1621 amorphous Si fast area detectors using the QXRD software for signal readout (Rothkirch et al., 2013, Jenings, 1997). Sample to detector distance and tilting of the detector with respect to the X-ray beam direction were calibrated using a CeO_2 powder standard (NIST 647a) and refined with the software Fit2D (Hammerseley, 1997). The typical image acquisition consisted in the summation of ten 1 s exposures.

Measurements were performed during compression and decompression. The maximum pressure reached was 41 GPa. Pressure was systematically determined by ruby fluorescence shift spectroscopy. The uncertainty on pressure was propagated from the estimated uncertainty on the wavelength of the ruby R_1 fluorescence line and corrected for the unavoidable non-hydrostaticity in the sample chamber at high pressures. The effect of nonhydrostatic stress was calculated based on the diffraction peaks broadening associated to microstrain in the sample. An X-ray diffraction line broadening model and a simple isotropic crystallite strain model (de Keijser et al., 1983; Lutterotti and Scardi, 1990) are implemented in MAUD software package (Lutterotti et al., 1999). The analysis was performed after subtraction of the instrumental broadening (calibrated based on the analysis of the x-ray diffraction of the CeO_2 standard). Sample microstrain was converted to stress by

using the isotropic Young's modulus $E = \frac{9K_H G_H}{3K_H + G_H}$ (where K_H is the Hill aggregate bulk modulus and G_H is the Hill aggregate shear modulus) determined from our ab initio computations (see section 3.2 Elasticity). X-ray diffraction images of Au were collected at selected pressures in experiment 1 and pressure determined by using the equation of state by (Heinz and Jeanloz, 1984) for comparison with the results from ruby. The pressures determined with the two methods were in agreement within reciprocal uncertainties.

Each X-ray diffraction image was then integrated with Fit2D and the lattice parameters of phase the 3.65 Å and of gold (in experiment 1) were refined with the Le Bail full-spectrum fit approach using MAUD software (**Fig. 2**). The estimated uncertainties of the unit-cell parameters refined with the Le Bail fit may be potentially biased by incorrect weighting of the strong background in our high-pressure x-ray diffraction images (for a general discussion of error estimated uncertainties see Post and Bish, 1989). In order to give a more conservative statement of the uncertainties we have performed parallel refinements based on individual peak fitting of few intense diffraction lines which are least affected by overlaps (002, 110, -110, 020, 021, 210, -210, 103, -103, 004, 220, -220, 114, 1-14, 130, -130, 204, 312, -312). The results of the two procedures are in very close agreement for all the spectra. Based on the positive comparison we have accepted the values of the unit cell parameters from Le Bail fit (which exploits the information from the whole diffraction image) and only corrected their uncertainties in order to have consistency with the results of the individual peaks fitting. The refined cell parameters of all the experimental runs are reported in the online supplementary material (**Tables ST1, ST2**).

171

172 ***2. 2. First principles simulation***

173 We performed *first-principles* quantum mechanical calculations based on
174 the density functional theory (DFT) (Hohenberg and Kohn, 1964, Kohn and Sham,
175 1965). DFT has been widely used to study the structure, energetics and elasticity
176 of geophysically relevant mineral phases (Cohen, 1987, Oganov et al., 2002,
177 Wentzcovitch and Stixrude, 2010). We have investigated the 3.65 Å phase with a
178 widely used approximation to the exchange-correlation functional: the
179 generalized gradient approximation (GGA) (Perdew and Wang, 1986, Perdew et
180 al., 1992, 1996). We have used the highly accurate projector augmented wave
181 method (PAW) (Kresse and Joubert, 1999) as implemented in the Vienna ab
182 initio simulation package (VASP) (Kresse and Hafner, 1993, Kresse and
183 Furthmuller, 1996a,b, Kresse and Joubert, 1999). For the first principles
184 simulations, we used a model crystal structure of 3.65 Å phase based on recent
185 studies (Wunder et al., 2011, 2012; Welch and Wunder, 2012). We determined
186 the energy-volume relationship of the 3.65 Å phase using GGA computations
187 with PAW methods. All computations were performed on the primitive unit cell
188 of 3.65 Å phase with $P2_1$ space group. We used an energy cut-off E_{cut}= 1000 eV
189 and a Monkhorst-Pack (Monkhorst and Pack, 1976) $2\times2\times2$ *k*-point mesh,
190 yielding 2 *k* points in the irreducible wedge of the Brillouin zone. A series of
191 convergence tests demonstrated that these computational parameters yield total
192 energies that are converged within 5 meV/atom. Previous studies have shown
193 that DFT captures the relevant physics of hydrous and hydrogen-bearing
194 nominally anhydrous minerals (Brodholt and Refson, 2000, Chheda et al., 2014,
195 Mainprice et al., 2007, 2008, Mookherjee and Tsuchiya, 2015, Panero and

196 Stixrude, 2004, Tsuchiya, 2013, Walker et al., 2007) with varying bond strengths
197 from strong hydroxyls to the weak interlayer forces (Fumagalli and Stixrude,
198 2007, Militzer et al., 2011, Mookherjee and Stixrude, 2006, 2009, Mookherjee
199 and Capitani, 2011, Stackhouse et al., 2004, Stixrude, 2002, Tsuchiya et al., 2002,
200 2005, 2008, Tsuchiya and Tsuchiya, 2009). Based on previous computational
201 studies GGA yields better results for hydrogen bearing mineral systems
202 (Mookherjee and Mainprice, 2014, Tsuchiya et al., 2005, 2008). In addition,
203 computational studies on molecular water (H_2O) and ice (Hamann, 1997) show
204 that the GGA method (Perdew et al., 1996) gives excellent results for energetics
205 and elasticity of hydrogen bearing systems. Hence, we calculated the full elastic
206 constant tensor of the 3.65 Å phase using the GGA (PAW) method. To calculate
207 the elasticity, we strained the lattice and let the internal degrees of freedom of
208 the crystal structure relax consistent with the symmetry: elastic constants are
209 obtained through the changes in stress tensor ($\underline{\underline{\sigma}}$) with respect to applied strain
210 ($\underline{\underline{\varepsilon}}$). We apply positive and negative strains of magnitude 1% in order to
211 accurately determine the stresses in the appropriate limit of zero strain. The
212 details of the method are outlined in (Stixrude and Lithgow-Bertelloni, 2005).
213 We have calculated the elastic anisotropy of 3.65 Å using the petrophysical
214 software (Mainprice, 1990).
215
216 **3. Results**
217 ***3. 1. Equation of state***
218 The X-ray diffraction patterns of the 3.65 Å phase from all the three
219 experimental runs consist of several tens of reflections, often overlapping, with
220 d-spacings ranging between 4.5 and 0.95 Å. The most intense and characteristic

(002) peak occurs at 3.65 Å. All the images present peaks from Ne pressure transmitting medium. In several diffraction images, mostly from experiment 1, we noticed diffraction peaks corresponding to the 10 Å phase. The presence of the 10 Å phase in the synthesis products was noted and discussed in a previous study (Wunder et al., 2011). Due to the very small size of the synchrotron X-ray beam, the sample region examined at each pressure was slightly different and the fraction of 10 Å phase detected in our measurements varied from image to image ranging from traces to about 10%.

Due to the complexity of the spectra we used Le Bail method, a full profile fitting approach, to refine the unit cell parameters of the 3.65 Å phase using the structural model proposed by Wunder et al., (2012). The Le Bail fits were complemented by single peaks fitting of the main diffraction lines of the 3.65 Å phase (see section 2.1). We measured the x-ray diffraction of the sample at ambient pressure in the diamond anvil cell, before Ne gas loading. The refined cell parameters are a_0 = 5.116 ± 0.005 Å, b_0 = 5.192 ± 0.005 Å, c_0 = 7.339 ± 0.010 Å, β_0 = 89.9 ± 0.1 degrees, in excellent agreement with the values a_0 = 5.1131 ± 0.0003 Å, b_0 = 5.1898 ± 0.0003 Å, c_0 = 7.3303 ± 0.004 Å, β_0 = 90.03 ± 0.01 degrees determined by Wunder et al. (2012). The cell parameters of all the experimental runs are reported in the supplementary sections (**Tables ST1, ST2**).

The compression behavior of the 3.65 Å phase is described using third- and fourth-order finite strain equations of state (Birch, 1960; 1978) and f_V - F_V relations (**Fig. 3**)

$$F_V = K_0 + \left(\frac{3K_0}{2}\right)\left[(K_0' - 4)f_V + \left(K_0K_0'' + (K_0' - 4)(K_0' - 3) + \left(\frac{35}{9}\right)\right)f_V^2\right] \quad (1)$$

where F_V is the normalized pressure, given by

$$F_V = \frac{P}{3f_V(1+2f_V)^{5/2}}, \quad (2)$$

f_V is the volume Eulerian finite strain

$$f_V = \frac{1}{2}\left[\left(\frac{V}{V_0}\right)^{-2/3} - 1\right], \quad (3)$$

V_0 is the zero-pressure volume, K_0 is the zero-pressure bulk modulus, K_0' is the pressure derivative of the bulk modulus, and the K_0'' is the second derivative of the bulk modulus with respect to pressure. In the third order finite strain equations of state (Birch, 1960; 1978) the term $\left(K_0K_0'' + (K_0' - 4)(K_0' - 3) + \left(\frac{35}{9}\right)\right)$ associated with the square of the volume Eulerian finite strain, f_V^2 in eq (1) is set to zero.

The linear bulk moduli (K_l) were determined using linear finite strain expression (Davies, 1974; Weaver, 1976; Meade and Jeanloz, 1990) and f_l-F_l relationships (**Fig. 3**)

$$F_l = K_l + m_l f_l \quad (4)$$

where F_l is the linear normalized pressure, given by

$$F_l = \frac{P}{f_l(1+2f_l)(1+2f_V)} \quad (5)$$

and f_l is the linear Eulerian finite strain, given by

$$f_l = \frac{1}{2}\left[\left(\frac{l}{l_0}\right)^{-2} - 1\right], \quad (6)$$

263 f_V is the volume Eulerian finite strain, as defined above in eq. (3), l and l_0 are the
264 length of a general lattice vector in the crystal and its length at zero pressure,
265 and m_l is related to elastic constants (Meade and Jeanloz, 1990).

266 In the fit of the experimental data, we fixed the ambient pressure unit cell
267 volume (and unit cell parameters) to the high precision values determined in our
268 previous study of the same material of the present high pressure study (Wunder
269 et al., 2012). The theoretical and experimental zero pressure volumes, V_0, are in
270 good agreement with $V_0^{PAWGGA} > V_0^{exp}$ by 3.8 % (the subscript *exp* refers to
271 experiments) (**Table 2, Fig. 3**). The third- and fourth-order Birch-Murnaghan
272 equation of state fits to the experimental data yield bulk moduli, K_0^{exp} of 83 (± 1)
273 GPa and 82 (± 1.7) GPa, respectively (**Table 2**)**.** The bulk modulus predicted with
274 static calculations K_0^{PAWGGA} is equal to 80 GPa, in very good agreement with the
275 experimental value (**Table 2, Fig. 3**). The predicted zero pressure lattice
276 parameters from static calculations are greater than the experimental
277 determinations by ~ 3.7, 2.2, and 0.6 % for a_0, b_0, and c_0, respectively (**Table 2,**
278 **Fig. 3**).
279
280 ***3. 2. Elasticity***
281 The 3.65 Å phase has a monoclinic space group ($P2_1$) (Wunder et al.,
282 2012) and hence there are 13 non-zero independent elastic constants c_{ij} in the
283 second order elastic tensor: c_{11}, c_{22}, and c_{33} are the principal elastic constants;
284 c_{44}, c_{55}, and c_{66} are the shear elastic constants; and c_{12}, c_{13}, c_{23}, c_{15}, c_{25}, c_{35}, and c_{46}
285 are the seven off-diagonal elastic constants (Nye, 1985). In this study, we have
286 calculated the full elastic constant tensor of the 3.65 Å phase as a function of

pressure. At low pressures, the principal components of elasticity are similar in magnitude, $c_{11} \sim c_{22} \sim c_{33}$. Upon compression the elastic constants stiffen at different rates and at high pressures the elastic constants increase in the order $c_{33} > c_{22} > c_{11}$ (**Fig. 4**). At low pressures, the shear elastic constants show the relation, $c_{66} > c_{55} \sim c_{44}$ and at high pressures, $c_{66} > c_{55} > c_{44}$. The pressure dependence of the elasticity data can be described with the finite strain formulation (Stixrude and Lithgow-Bertelloni, 2005) (**Table 3**).

$$c_{ijkl} = (1+2f_V)^{3.5}[c_{ijkl0} + b_1 f_V + 2b_2 f_V^2] - P\Delta_{ijkl}, \quad (7)$$

where, f_V is the finite Eulerian strain as defined in eq (3)

$$b_1 = 3K_0(c'_{ijkl0} + \Delta_{ijkl}) - 7c_{ijkl0}, \quad (8)$$

$$b_2 = 9K_0^2 c''_{ijkl0} + 3K'_0(b_1 + 7c_{ijkl0}) - 16b_1 - 49c_{ijkl0}, \quad (9)$$

and $\Delta_{ijkl} = -\delta_{ij}\delta_{kl} - \delta_{ik}\delta_{jl} - \delta_{il}\delta_{jk}$ (10)

where c'_{ijkl0} and c''_{ijkl0} are the first and second derivatives of c_{ijkl}, with respect to pressure at ambient conditions. Δ_{ijkl} is equal to -3 for the principal constants (c_{iiii} in full tensor and c_{ii} in Voigt notation, with i= 1, 2, 3), -1 for the off-diagonal elastic constants (c_{iijj} in full tensor and c_{ij} in Voigt notation, with i=1, 2, 3, i≠j), -1 for the shear constants (c_{ijij} in full tensor notation with i=1, 2, 3, i≠j and c_{ij} in Voigt notation with i= 4, 5, 6, i=j), and 0 otherwise. δ_{ij} is the Kronecker delta (δ_{ij} = 1 for i=j, and δ_{ij} = 0, for i≠j).

The isotropic bulk (K) and shear (G) moduli are determined using the relations

$$K_{Voigt} = \left(\frac{1}{9}\right)\left[c_{11} + c_{22} + c_{33} + 2(c_{12} + c_{13} + c_{23})\right], \quad (11)$$

$$K_{Reuss} = \left[s_{11} + s_{22} + s_{33} + 2(s_{12} + s_{13} + s_{23})\right]^{-1}, \quad (12)$$

$$G_{Voigt} = \left(\frac{1}{15}\right)\left[c_{11} + c_{22} + c_{33} - (c_{12} + c_{13} + c_{23}) + 3(c_{44} + c_{55} + c_{66})\right], \quad (13)$$

$$\text{and } G_{Reuss} = (15)\left[4(s_{11} + s_{22} + s_{33}) - (s_{12} + s_{13} + s_{23}) + 3(s_{44} + s_{55} + s_{66})\right]^{-1} \quad (14)$$

s_{ijkl} are the elastic compliances (the elastic compliance tensor is related to the elastic constant tensor as $s_{ijkl}c_{klmn} = \delta_{im}\delta_{jn}$) and Voigt notation for the compliance tensor is used. Average moduli (**Table 3**) are calculated as average of Voigt and Reuss bounds (Hill average).

3. 3. Structure and Hydrogen bond

Several hydrogen bearing condensed matter phases including ices and hydrous mineral phases undergo symmetrization of hydrogen bonding upon compression. For instance, at around 60 GPa, ice VII, and ice VIII transform to ice X (Goncharov et al., 1996; Benoit et al., 1998). A similar transition occurs at ~5 GPa for β-CrOOH (Jahn et al., 2012), and at ~16-24 GPa for δ-AlOOD [*Sano-Furukawa et al*., 2008]. DFT simulations on phase D also predicted hydrogen bond symmetrization at 40 GPa (Tsuchiya et al., 2002). Experimental investigations using infrared spectroscopy however, did not document hydrogen bond symmetrization up to 40 GPa (Shieh et al., 2009). Extrapolation of vibrational frequencies of hydroxyl stretch and hydrogen bonding indicated that a hydrogen bond symmetrization is likely at higher pressure around 112 GPa (Shieh et al., 2009). In a more recent X-ray diffraction study of phase D, a kink in pressure-volume results at 40 GPa was interpreted as related to hydrogen bond symmetrization (Hushur et al., 2011). The difference in the hydrogen bond symmetrization pressure based on infrared and X-ray diffraction studies could in

part be related to the difference in the exact stoichiometry of the phase D samples. The stoichiometry of the phase D used in X-ray diffraction study is $Mg_{1.0}Si_{1.7}H_{3.0}O_6$ (Hushur et al., 2011) whereas the stoichiometry of phase D used in the high-pressure infrared spectroscopic study by Shieh et al. (2009) is inferred to be between $Mg_{1.11}Si_{1.89}H_{2.22}O_6$ (Yang et al., 1997) and $Mg_{1.84}Si_{1.73}H_{2.81}O_6$ (Ohtani et al., 1997). These changes in the local arrangements of the protons in the crystal structures of DHMS and related mineral phases have serious effects on the bulk physical properties including bulk and shear modulus (Tsuchiya and Tsuchiya, 2009, Hushur et al., 2011).

Based on our *first principles* simulations on the 3.65 Å phase, the hydroxyl bond length d(O-H) increases by 12 % from ~0.99 to 1.14 Å upon compression to ~50 GPa, whereas in the same pressure interval, the corresponding d(O---O) distance decrease by 55 % from 1.80 to 1.17 Å (**Fig. 5**). At around ~60 GPa the hydrogen atom is located in the center of the d(O---O) unit (**Fig. 5**), thus we observe symmetrization of the hydrogen bonding. The O-H---O angles continuously decrease upon compression. However, in the 3.65 Å phase, the hydrogen bond symmetrization occurs at a pressure (~60 GPa) exceeding its thermodynamic stability (Wunder et al., 2011; 2012).

The Mg-Si-O framework of the 3.65 Å phase responds to increasing pressure by two mechanism- (a) compression of octahedral units and (b) rigid rotation of the octahedral units. The volume of the MgO_6 and SiO_6 octahedral units reduces continuously upon compression, not reflecting the non-linear dependence of the hydroxyl groups. The pressure dependence of the octahedral units can be expressed by a finite strain expression with K_0 = 102.0 GPa, K_0' = 3.0 and V_0 = 12.72 Å^3 for MgO_6 units and K_0 = 234.9 GPa, K_0' = 2.6 and V_0 = 7.99 Å^3 for

the SiO_6 units. However, the octahedral rigid rotation as manifested by the average Mg-O-Si angle shows linear behavior till the hydrogen bonds symmetrize at ~60 GPa (**Fig. 5**). The absence of the A cation in this hydroxide perovskite structure allows for greater octahedral rigid rotation than observed for perovskite with the A cation site occupied, such as the $MgSiO_3$. As a consequence the bulk modulus of the 3.65 Å phase is more than 60% softer than that of $MgSiO_3$ perovskite (**Table 4**). The shear modulus of the phase 3.65 Å, G_H = 65.1 GPa is more than 60% softer than that of $MgSiO_3$ perovskite with G_H = 175 GPa (Sinogeikin et al., 2004).

4. Discussion

Bulk elastic properties of mineral phases are sensitive to chemistry, in particular water content (Smyth and Jacobsen, 2006). A bulk-modulus (K_0)-density (ρ_0) systematics for major mantle phases, nominally anhydrous phases, and hydrous phases in the MgO-SiO_2-H_2O system (MSH) reveals a positive correlation (**Fig. 6**). As the water content increases within various hydrous phases, significant reduction of density and bulk modulus is observed. Mineral phases with silicon atom in octahedral coordination [Si^{VI}], such as stishovite, and bridgmanite (perovskite) have greater density and bulk modulus (**Fig. 6**). Among the hydrous phases, layered hydrous magnesium silicates (LHMS) such as antigorite, talc, 10 Å phase and brucite have lower density and bulk moduli. In contrast, DHMS phases such as phase D with silicon atom in octahedral coordination [Si^{VI}] have high both higher density and bulk modulus. Although, the 3.65 Å phase also has silicon atom in the octahedral coordination [Si^{VI}], the amount of water content in 3.65 Å phase is significantly greater than that in

phase D, other DHMS phases, and LHMS phases. This is the likely cause of the low density of 3.65 Å phase (**Fig 6**; **Table 4**). The bulk modulus of 3.65 Å phase lies in between LHMS and DHMS phases.

The bulk sound velocity (V_Φ)-density (ρ_0) systematics also exhibits a positive correlation for the mineral phases in the $MgSiO_3$-H_2O join. Among the major mantle phases with $MgSiO_3$ stoichiometry, the density and bulk sound velocity of the upper mantle phase clinoenstatite is the lowest followed by majorite garnet, stable at the transition zone conditions, and the lower mantle phase- bridgmanite (perovskite) being the densest among the three. The 3.65 Å phase, stable in the lower part of the upper mantle, has a density lower than clinoenstatite (**Fig. 6**). The V_Φ - ρ systematics with a linear correlation: $V_\Phi = 0.19 + 1.87\rho$, could be used to constrain the degree of mantle hydration in the cores of the cold subduction zones where temperature could be low enough to allow the presence of 3.65 Å phase (Wunder et al., 2012).

5. Implications

The appearance of 3.65 Å phase at 9-10 GPa, i.e., 270-330 km, from the breakdown of 10 Å phase might be related to the observed seismic 'X-discontinuity' (Revenaugh and Jordan, 1991). The X-discontinuity, although not a global discontinuity, is quite widespread and has been observed at several locations word wide in the depth range of 270-330 km (Revenaugh and Jordan, 1991, Deuss and Woodhouse, 2002, Bageley and Revenaugh, 2008 and references therein). Based on the varying depth, it is likely that the X-discontinuity might have multiple origins (Bageley and Revenaugh, 2008).

406 Several mineralogical transitions have been invoked to explain the X-
407 discontinuity, including phase transitions, such as from orthoenstatite (OEn) to
408 high-pressure clinoenstatite (HPCen) (Angel et al., 1992, Woodland, 1998,
409 Jacobsen et al., 2010) and from coesite (Coe) to stishovite (St) transition
410 (Williams and Revenaugh, 2005, Pushcharvosky and Pushcharvosky, 2012, Chen
411 et al., 2015). Formation of stishovite in eclogites requires either presence of
412 excess silica or exsolution of silica component from calcium clinopyroxene
413 (Knapp et al., 2013). However, a recent experimental study suggests that
414 exsolution of silica from calcium clinopyroxene is not a feasible mechanism to
415 explain X-discontinuity (Knapp et al., 2013). Other proposed explanations
416 include the appearance of anhydrous phase B ($Mg_{14}Si_5O_{24}$) from a reaction of
417 olivine (Mg_2SiO_4) and periclase (MgO) (Ganguly and Frost, 2006) or the forming
418 of hydrous phases such as phase A [$Mg_7Si_2O_{14}H_6$] (Liu, 1987, Revenaugh and
419 Jordan, 1991).

420 The LHMS such as antigorite and talc that are stable at shallower depths
421 along the subduction zone exhibit strong elastic anisotropy which is defined as
422 $AV_{P,S} = 100(V_{P,S\,Max} - V_{S,P\,Min})/\langle V_{P,S}\rangle$, where $V_{P,S\,Max}$ and $V_{P,S\,Min}$ are the maximum
423 and minimum (orientation dependent) compressional or shear acoustic velocity
424 and $\langle V_{P,S}\rangle$ is the average P, -S wave velocity (Mainprice et al., 2008; Mookherjee
425 and Capitani, 2011; Bezacier et al., 2013). The strong anisotropy, in particular
426 shear anisotropy (AV_S) could explain the large shear wave delay time observed
427 in the mantle wedges in certain subduction zone settings such as Ryukyu
428 (Katayama et al., 2009). Upon compression the shear (AV_S) and compressional
429 (AV_P) elastic anisotropies of LHMS reduce significantly. The X-discontinuity

might also be related to a discontinuity in seismic anisotropy owing to the considerable difference in the elastic anisotropies of LHMS at shallower depths and DHMS at larger depths (**Fig. 7**). The DHMS phases such as phase A (Sanchez-Valle et al., 2008), superhydrous phase B (Pacalo and Weidner, 1996), and phase D (Mainprice et al., 2007; Rosa et al., 2012) phase exhibit lower elastic anisotropy. However, in comparison to the DHMS phases, 3.65 Å phase has 10%(?) higher shear elastic anisotropy and its anisotropy increases upon compression (**Fig. 7**). A detailed understanding of the slip system activities and high-pressure deformation fabrics of DHMS is required to relate single crystal elastic anisotropy to the seismological observation.

5. Acknowledgement

MM is supported by the US National Science Foundation grant- EAR 1250477. MM acknowledges computing resources (request # EAR130015) from the Extreme Science and Engineering Discovery Environment (XSEDE), which is supported by National Science Foundation grant number OCI-1053575. HM is supported by the Deutsche Forschungsgemeinschaft DFG grants SP 1216/3-1 and MA4534/3-1.

Reference

Abers, G. (2005) Seismic low-velocity layer at the top of subducting slabs: observations, predictions, and systematics, *Phys. Earth Planet. Int.*, 149, 7-29.

Angel, R. J., Chopelas, A., and Ross, N. L. (1992) Stability of high-density clinoenstatite at upper-mantle pressures. Nature, 358, 322–324.

455 Asahara, Y., Murakami, M., Ohishi, Y., Hirao, N., and Hirose, K. (2010) Sound
456 velocity measurement in liquid water up to 25 GPa and 900 K:
457 Implications for densities of water at lower mantle conditions. Earth and
458 Planetary Science Letters, 289, 479-485.
459 Bagley, B., and Revenaugh, J. (2008) Upper mantle seismic shear discontinuities
460 of the Pacific. Journal of Geophysical Research, 113, B12301.
461 Benoit, M., Dominik, M., and Parrinello, M. (1998) Tunneling and zero-point
462 motion in high-pressure ice. Nature, 392, 258-261.
463 Bezacier, L., Reynard, B., Bass, J. D., Sanchez-Valle, C., and Van de Moortèle, B.
464 (2010) Elasticity of antigorite, seismic detection of serpentinites, and
465 anisotropy in subduction zones. Earth and Planetary Science Letters, 289,
466 198-208.
467 Bezacier, L., Reynard, B., Cardon, H., Montagnac, G., and Bass, J. D. (2013) High-
468 pressure elasticity of serpentine and seismic properties of the hydrated
469 mantle wedge. Journal of Geophysical Research, 118, 527–535.
470 Bina, C. R., and Navrotsky, A. (2000) Possible presence of high-pressure ice in
471 cold subducting slabs. Nature, 408, 844-847.
472 Birch, F. (1960) The velocity of compressional waves in rocks to 10-kilobars. 1.
473 Journal of Geophysical Research, 65, 1083-1102.
474 Birch, F. (1978) Finite Strain Isotherm and Velocities for Single-Crystal and
475 Polycrystalline NaCl at High-Pressures and 300 K. Journal of Geophysical
476 Research, 83, 1257-1268.
477 Bostock, M. G., Hyndman, R. D., Rondenay, S., and Peacock, S. M. (2002) An
478 inverted continental Moho and serpentinization of the forearc mantle.
479 Nature, 417, 536-538.

480 Brodholt, J. P., and Refson, K. (2000) An ab initio study of hydrogen in forsterite
481 and a possible mechanism for hydrolytic weakening. Journal of
482 Geophysical Research, 105, 18,977-18,982.
483 Bromiley, G. D., and Pawley, A. R. (2003) The stability of antigorite in the systems
484 MgO-SiO_2-H_2O (MSH) and MgO-Al_2O_3-SiO_2-H_2O (MASH): the effect of Al^{3+}
485 substitution on high-pressure stability. American Mineralogist, 88, 99-108.
486 Brudzinski, M., Thurber, C. H., Hacker, B. R., and Engdahl, E. R. (2007) global
487 prevalence of double Benioff zones. Science, 316, 1472-1474.
488 Chantel, J., Mookherjee, M., and Frost, D. J. (2012) The elasticity of lawsonite at
489 high pressure and the origin of low velocity layers in subduction zones.
490 Earth and Planetary Science Letters, 349-350, 116-125.
491 Chen, T., Gwanmesia, G. D., Wang, X., Zou, Y., Liebermann, R. C., Michaut, C., and
492 Li, B. (2015) Anomalous elastic properties of coesite at high pressure and
493 implications for the upper mantle X-discontinuity. Earth and Planetary
494 Science Letters, 412, 42-51.
495 Chheda, T. D., Mookherjee, M., Mainprice, D., dos Santos, A. M., Molaison, J. J.,
496 Chantel, J., Manthilake, G., and Bassett, W. A. (2014) Structure and
497 elasticity of phlogopite under compression: Geophysical implications.
498 Physics of the Earth and Planetary Interiors, 233, 1-12.
499 Clark, S. M., Gleason, A. E., Pawley, A. R., Parry, S., and Walter, M. J. (2004) The
500 phase diagram of talc, 10 Å phase and 3.65 Å phase. American
501 Geophysical Union, Abstract, 2004AGUFM.T41B1177C.
502 Cohen, R. E. (1987) Elasticity and equation of state of $MgSiO_3$ perovskite.
503 Geophysical Research Letters, 14, 1053-1056.
504 Comodi, P., Fumagalli, P., Nazzareni, S., and Zanazzi, P. F. (2005) The 10 Å phase:

505 Crystal structure from single-crystal X-ray data. American Mineralogist,
506 90, 1012-1016.
507 Comodi, P., Cera, F., Dubrovinsky, L., and Nazzareni, S. (2006) The high-pressure
508 behavior of the 10 Å phase: A spectroscopic and diffractometric study up
509 to 42 GPa. Earth and Planetary Science Letters,246, 444-457.
510 Davies, G. F. (1974). Effective elastic moduli under hydrostatic stress-I.
511 quasiharmonic theory. Journal of Physics and Chemistry of Solids, 35,
512 1513–1520.
513 de Keijser, Th. H., Langford, J. I., Mittemejier, E. J., and Vogels, A. B. P. (1982) Use
514 of the Voigt function in a single-line method for the analysis of X-ray
515 diffraction line broadening. Journal of Applied Crystallography, 15, 308-
516 314.
517 de Keijser, Th. H., Mittemejier, E. J., and Rozendaal, H. C. F. (1983) The
518 determination of crystallite-size and lattice-strain parameters in
519 conjunction with the profile-refinement method for the determination of
520 crystal structures. Journal of Applied Crystallography, 16, 309-316.
521 Deuss, A., and Woodhouse, J. H. (2002) A systematic search for mantle
522 discontinuities using SS-precursors. Geophysical Research Letters,
523 29,1249.
524 Frost, D. J. (2006) The stability of mantle hydrous phases. Reviews of Mineralogy
525 and Geochemistry, 62, 243-271.
526 Fumagalli, P., and Poli, S. (2005) Experimentally determined phase relations in
527 hydrous peridotites to 6.5 GPa and their consequences on the dynamics of
528 subduction zones. Journal of Petrology, 46, 555-578.

529 Fumagalli, P., and Stixrude, L. (2007) The 10 Angstrom phase at high pressure by
530 first principles calculations and implications for the petrology of
531 subduction zones. Earth and Planetary Science Letters, 260, 212-226.
532 Ganguly, J., and Frost, D. J. (2006) Stability of anhydrous phase B: Experimental
533 studies and implications for phase relations in subducting slab and the X
534 discontinuity in the mantle. Journal of Geophysical Research, 111, B06203.
535 Gleason, A. E., Parry, S. A., Pawley, A. R., Jeanloz, R., and Clark, S. M. (2008)
536 Pressure-temperature studies of talc plus water using X-ray diffraction.
537 American Mineralogist, 93, 1043-1050.
538 Goncharov, A. F., Struzhkin, V. V., Somayazulu, M. S., Hemley, R. J., and Mao, H. K.
539 (1996) Compression of ice to 210 gigapascals: Infrared evidence for a
540 symmetric hydrogen-bonded phase. Science, 273, 218-220.
541 Hacker, B. R. (2008) H_2O subduction beyond arcs. Geochemistry Geophysics
542 Geosystems, 9, Q03001.
543 Hamann, D. R. (1997) H_2O hydrogen bonding in density-functional theory.
544 Physical Review B, 55, R10157-R10160,
545 Hammerseley, A. P. (1997) FIT2D: An introduction and overview, European
546 Synchroton Radiation Facility Internal Report.
547 Heinz, D. L., and Jeanloz, R. (1984) The equation of state of the gold calibration
548 standard. Journal of Applied Physics, 55, 885-893.
549 Hohenberg, P., and Kohn, W. (1964) Inhomogeneous Electron Gas. Physical
550 Review B, 136, B864-B871.
551 Hushur, A., Manghnani, M. H., Smyth, J. R., Williams, Q., Hellebrand, E., Lonappan,
552 D., Ye, Y., Dera P., and Frost, D.J. (2011) Hydrogen bond symmetrization

553 and equation of state of phase D. Journal of Geophysical Research, 116,
554 B06203.
555 Iwamori, H. (1998) Transportation of H_2O and melting in subduction zones.
556 Earth and Planetary Science Letters, 160, 65-80.
557 Iwamori, H. (2004) Phase relations of peridotites under H_2O-saturated
558 conditions and ability of subducting plates for transportation of H_2O.
559 Earth and Planetary Science Letters, 227, 57-71.
560 Iwamori, H. (2007). Transportation of H_2O beneath the Japan arcs and its
561 implications for global water circulation. Chemical Geology, 239, 192-198.
562 Jacobsen, S. D., Liu, Z., Boffa Ballaran, T., Littlefield, E. F., Ehm, L., and Hemley, R. J.
563 (2010) Effect of H_2O on upper mantle phase transitions in $MgSiO_3$: Is the
564 depth of the seismic X-discontinuity an indicator of mantle water content?
565 Physics of the Earth and Planetary Interiors, 183, 234-244.
566 Jahn, S., Wunder, B., Koch-Müller, M., Tarrieu, L., Pöhle, M., Watenphul, A., and
567 Taran, M. N. (2012) Pressure-induced hydrogen bond symmetrization in
568 guyanaite, β-CrOOH: Evidence from spectroscopy and *ab initio*
569 simulations. European Journal of Mineralogy, 24, 839-850.
570 Jennings, G. (1997) QXRD: Readout software for flat panel x-ray detectors.
571 Structural Science Group, Advanced Photon Source, Argonne National
572 Laboratory, [http://sourceforge.net/projectsqxrd/].
573 Jiang, F., Gwanmesia, G. D., Dyuzheva, T. I., and Duffy, T. S. (2009) Elasticity of
574 stishovite and acoustic mode softening under high pressure by Brillouin
575 scattering. Physics of the Earth and Planetary Interiors, 172, 235-240.

576 Jiang, F., Speziale, S., and Duffy, T. S. (2006) Single-crystal elasticity of brucite,
577 $Mg(OH)_2$, to 15 GPa by Brillouin scattering. American Mineralogist, *91*,
578 1893-1900.
579 Jung, H. (2011) Seismic anisotropy produced by serpentine in mantle wedge.
580 Earth and Planetary Science Letters, 307, 535–543.
581 Karki, B. B., Stixrude, L., and Crain, J. (1997) Ab initio elasticity of three high-
582 pressure polymorphs of silica. Geophysics Research Letters, 24, 3269-
583 3272.
584 Katayama, I., Hirauchi, K.-i., Michibayashi, K., and Ando, J. (2009) Trench-parallel
585 anisotropy produced by serpentine deformation in the hydrated mantle
586 wedge. Nature, 461, 1114-1117.
587 Kawamoto, T. (2006) Hydrous phases and water transport in the subducting
588 slab. Reviews of Mineralogy and Geochemistry, 62, 273-289.
589 Kell, G. S. (1975) Density, thermal expansivity, and compressibility of liquid
590 water from 0^o to 150 ^{o}C: Correlations and tables for atmospheric pressure
591 and saturation reviewed and expressed on 1968 temperature scale.
592 Journal of Chemical and Engineering Data, 20, 97-105.
593 Keppler, H., and Bolfan-Casanova, N. (2006) Thermodynamics of water solubility
594 and partitioning. Reviews of Mineralogy and Geochemistry, 62, 193-230.
595 Kim, Y., Clayton, R. W., and Jackson, J. M. (2012) Distribution of hydrous minerals
596 in the subduction system beneath Mexico. Earth and Planetary Science
597 Letters, 341-344, 58-67.
598 Kim, Y., Clayton, R. W., Asimow, P. D., and Jackson, J. M. (2013) Generation of talc
599 in the mantle wedge and its role in subduction dynamics in central Mexico.
600 Earth and Planetary Science Letters, 384, 81-87.

601 Kleppe, A. K., Welch, M. D., Chrichton, W. A., and Jephcoat, A. P. (2012) Phase
602 transitions in hydroxide perovskites: a Raman spectroscopic study of
603 stottite, $FeGe(OH)_6$, to 21 GPa. Mineralogical Magazine, 76, 949-962.
604 Knapp, N., Woodland, A. B., and Klimm, K. (2013) Experimental constraints in the
605 CMAS system on the Ca-Eskola content of eclogitic clinopyroxene.
606 European Journal of Mineralogy, 25, 579-596.
607 Kohn, W., and Sham, L. J. (1965) Self-Consistent Equations Including Exchange
608 and Correlation Effects. Physical Review, 140, 1133-1138.
609 Kresse, G., and Furthmüller, J. (1996a) Efficiency of ab-initio total energy
610 calculations for metals and semiconductors using a plane-wave basis set.
611 Computational Material Science, 6, 15-50.
612 Kresse, G., and Furthmüller, J. (1996b) Efficient iterative schemes for ab initio
613 total-energy calculations using a plane-wave basis set. Physical Reviews B,
614 54, 11169-11186.
615 Kresse, G., and Hafner, J. (1993) Ab initio Molecular-Dynamics for Liquid-Metals.
616 Physical Reviews B, 47, 558-561.
617 Kresse, G., and Joubert, D. (1999) From ultrasoft pseudopotentials to the
618 projector augmented-wave method. Physical Reviews B, 59, 1758-1775.
619 Kung, J., Li, B., Uchida, T., and Wang, Y. (2005) In-situ elasticity measurement for
620 the unquenchable high-pressure clinopyroxene phase: Implication for the
621 upper mantle. Geophysics Research Letters, 32, L01307.
622 Libowitzky, E. and Rossman, G. R. (1997) An IR absorption calibration for water
623 in minerals. American Mineralogist, 82, 1111–1115.
624 Liermann, H.-P., Morgenroth, W.m Ehnes, A., Berghäuser, Winkler, B., Franz, H.,
625 Weckert, E. (2010) The extreme conditions beamline at PETRA III:

626 Possibilities to conduct time resolved monochromatic diffraction
627 experiments in dynamic and laser heated DAC. Journal of Physics:
628 Conference Series, 215, 012029, 1-6.
629 Liu, L.-G. (1986) Phase transformations in serpentine at high pressures and
630 temperatures and implications for subducting lithosphere. Physics of the
631 Earth and Planetary Inter, 42, 255–262.
632 Liu, L.-G. (1987) Effects of H_2O on the phase behavior of the forsterite-enstatite
633 system at high pressures and temperatures and implications for the Earth.
634 Physics of the Earth and Planetary Inter, 49, 142-167.
635 Liu, J., Topor, L., Zhang, J., Navrotsky, A., Liebermann, R. C. (1996) Calorimetric
636 study of the coesite-stishovite transformation and calculation of the phase
637 boundary. Physics and Chemistry of Minerals, 23, 11-16.
638 Long, M. D., and Silver, P. G. (2008) The subduction zone flow field from seismic
639 anisotropy: A global view. Science, 319, 315–318.
640 Lutterotti, L., Matthies, S., and Wenk, H.-R. (1999) MAUD: a friendly Java program
641 for material analysis using diffraction. Int. Union Crys. (IUCr): Newsletter
642 of the Commission on Powder Diffraction, 21, 14-15.
643 Lutterotti, L., and Scardi, P. (1990) Simultaneous structure and size-strain
644 refinement by the Rietveld method. Journal of Applied Crystallography,
645 23, 246-252.
646 Mainprice, D. (1990) A fortran program to calculate seismic anisotropy from the
647 lattice preferred orientation of minerals. Computers and Geoscience, 16,
648 385-393.
649 Mainprice, D., Le Page, Y., Rodgers, J., and Jouanna, P. (2007) Predicted elastic
650 properties of the hydrous D phase at mantle pressures: Implications for

651 the anisotropy of subducted slabs near 670-km discontinuity and in the
652 lower mantle. Earth and Planetary Science Letters, 259, 283-296.
653 Mainprice, D., Le Page, Y., Rodgers, J., and Jouanna, P. (2008) Ab initio elastic
654 properties of talc from 0 to 12 GPa: Interpretation of seismic velocities at
655 mantle pressures and prediction of auxetic behavior at low pressure.
656 Earth and Planetary Science Letters, 274, 327-338.
657 Mao, H. K., and Bell, P. M. (1980) Design and operation of a diamond-window,
658 high-pressure cell for the study of single-crystal samples loaded
659 cryogenically. Carnegie Inst. Washington Yearbook, *79*, 409-411.
660 Mao, H. K., and Xu, J., and Bell, P. M. (1986) Calibration of the ruby pressure
661 gauge to 800 kbar under quasi-hydrostatic conditions. Journal of
662 Geophysical Research, 91, 4673-4676.
663 Mao, Z., Jacobsen, S. D., Jiang, F., Smyth, J. R., Holl, C. M., and Duffy, T.
664 S. (2008) Elasticity of hydrous wadsleyite to 12 GPa: Implications for
665 Earth's transition zone. Geophysical Research Letters, 35, L21305.
666 Mao, Z., Jacobsen, S. D., Jiang, F., Smyth, J. R., Holl, C., Frost, D. J., and Duffy, T. S.
667 (2010) Velocity crossover between hydrous and anhydrous forsterite at
668 high pressures. Earth and Planetary Science Letters, 293, 250-258.
669 Mao, Z., Lin, J. F., Jacobsen, S. D., Duffy, T. S., Chang, Y.-Y., Smyth, J. R., Frost, D. J.,
670 Hauri, E. H., and Prakapenka, V. B. (2012) Sound velocity of hydrous
671 ringwoodite to 16 GPa and 673 K. Earth and Planetary Science Letters,
672 331-332, 112-119.
673 Meade, C., and Jeanloz, R. (1990) Static compression of $Ca(OH)_2$ at room
674 temperature: Observation of amorphization and equation of state
675 measurements to 10.7 GPa. Geophysical Research Letters, 17, 1157-1160.

Militzer, B., Wenk, H.-R., Stackhouse, S., and Stixrude, L. (2011) First-principles calculation of the elastic moduli of sheet silicates and their application to shale anisotropy. American Mineralogist, 96, 125-137.

Monkhorst, H. J., and Pack, J. D. (1976) Special points for Brillouin-zone integrations. Physical Review B, 13, 5188-5192.

Mookherjee, M., and Bezacier, L. (2012) The low velocity layer in subduction zone: Structure and elasticity of glaucophane at high pressure. Physics of the Earth and Planetary Interiors, 208-209, 50-58.

Mookherjee, M., and Capitani, G. C. (2011) Trench parallel anisotropy and large delay times: Elasticity and anisotropy of antigorite at high pressure. Geophysical Research Letters, 38, L09315, doi:10.1029/2011GL047160.

Mookherjee, M., and Mainprice, D. (2014) Unusually large shear wave anisotropy for chlorite in subduction zone settings. Geophysical Research Letters, 41, 1506-1513.

Mookherjee, M., and Stixrude, L. (2006) High-pressure proton disorder in brucite. American Mineralogist, 91, 127-134.

Mookherjee, M., and Stixrude, L. (2009) Structure and elasticity of serpentine at high-pressure. Earth and Planetary Science Letters, 279, 11-19.

Mookherjee, M., and Tsuhiya, J. (2015) Elasticity of superhydrous phase, B, $Mg_{10}Si_3O_{14}(OH)_4$, Physics of the Earth and Planetary Interiors, 238, 42-50.

Nye, J. F. (1985) Physical properties of crystals. Clarendon, Oxford University Press.

Oganov, A. R., Brodholt, J. P., and Price, G. D. (2002) Ab initio theory of thermoelasticity and phase transitions in minerals. Energy Modelling in Minerals, European Mineralogical Union Notes in Mineralogy, 4, 83-170.

Ohtani, E., Mizobata, H., Kudoh, T.,Nagase, T., Arashi, H., Yurimoto, H., and Miyagi, I. (1997) A new hydrous silicate, a water reservoir, in the upper part of the lower mantle. Geophysics Research Letters, 24, 1047–1050.

Pacalo, R. E. G., and Gasparik, T. (1990) Reversals of the orthoenstatite-clinoenstatite transition at high pressures and temperatures. Journal of Geophysical Research, 95, 15853-15858.

Pacalo, R. E. G., and Weidner, D. (1996) Elasticity of superhydrous phase B, Physics and Chemistry of Minerals, 23, 520-525.

Panero, W. R., and Stixrude, L. P. (2004) Hydrogen incorporation in stishovite and symmetric hydrogen bonding in δ-AlOOH. Earth and Planetary Science Letters, 221, 421-431.

Pawley, A. R., and Wood, B. J. (1995) The high-pressure stability of talc and 10-Å phase: potential storage sites for H_2O in subduction zones. American Mineralogist, 80, 998–1003.

Pawley, A. R., Clark, S. M., and Chinnery, N. J. (2002) Equation of state measurements of chlorite, pyrophyllite, and talc. American Mineralogist, 87, 1172-1182.

Pawley, A. R., Chinnery, N. J., Clarck, S. M., and Walter, M. J. (2011) Experimental study of the dehydration of 10-Å phase, with implications for its H_2O content and stability in subducted lithosphere. Contributions to Mineralogy and Petrology, 162, 1279-1289.

Pawley, A. R., (2003) Chlorite stability in mantle peridotite: the reaction clinochlore + enstatite = forsterite + pyrope + H_2O. Contributions to Mineralogy and Petrology, , 144, 449-456.

Pearson, D. G., Brenker, F. E., Nestola, F., McNeill, J., Nasdala, L., Hutchinson, M. T., Matveev, S., Mather, K., Silversmit, G., Schmitz, S., Vekemans, B., and Vincze, L. (2014) Hydrous mantle transition zone indicated by ringwoodite included within diamond. Nature, 507, 221-224.

Perdew, J. P., and Wang, Y. (1986) Accurate and simple density functional for the electronic exchange energy: Generalized gradient approximation, Physical Review, B, 33, 8800-8802.

Perdew, J. P., Chevary, J. A., Vosko, S. H., Jackson, K. A., Pederson, M. R., Singh, D. J., and Fiolhais, C. (1992) Atoms, molecules, solids, and surfaces: Applications of the generalized gradient approximation for exchange and correlation. Physical Review, B, 46, 6671-6687.

Perdew, J. P., Burke, K., and Erzerhof, M. (1996) Generalized gradient approximation made simple. Physical Review Letters, 77, 3865-3868.

Post, J. E., and Bish, D. L. (1989) Rietveld refinement of crystal structures using powder diffraction data. Review of Mineralogy and Geochemistry, 20, 276-308.

Prewitt, C. T. and Downs, R. T. (1998) High-Pressure Crystal Chemistry. Review of Mineralogy and Geochemistry, 37, 283-317.

Pushcharovsky, D. Y., and Pushcharovsky, Yu. M. (2012) The mineralogy and the origin of deep geospheres: A review, Earth-Science Reviews, 113, 94-109.

Revenaugh, J., and Jordan, T. H. (1991) Mantle layering from ScS reverberations: 3. The upper mantle. Journal Geophysics Research, 96, 19781-19810.

Rosa, A. D., Sanchez-Valle, C. and Ghosh, S. (2012) Elasticity of phase D and its implication for the degree of hydration of deep subducted slabs. Geophysics Research Letters, 39, L06304.

Rothkirch, A., Gatta, G. D., Meyer, M., Merkel, S., Merlini, M., and Liermann, H.-P. (2013) Single-crystal diffraction at the Extreme Conditions beamline P02.2: procedure for collecting and analyzing high-pressure single-crystal data. Journal of Synchroton Radiation, 20, 1-10.

Sanchez-Valle, C., Sinogeikin, S. V., Smyth, J. R., and Bass, J. D., (2008), Sound velocities and elasticity of DHMS phase A to high pressure and implications for seismic velocities and anisotropy in subducted slab. Physics of the Earth and Planetary Interiors, 170, 229-239.

Sano-Furukawa, A., Komatsu, K., Vanpetghem, C. B. and Ohtani, E., (2008). Neutron diffraction study of δ-AlOOD at high pressure and its implication for symmetrization of the hydrogen bond. American Mineralogist, 93, 1558-1567.

Shieh, S. R., Duffy, T. S., Liu, Z., and Ohtani, E., (2009) High-pressure infrared spectroscopy of the dense hydrous magnesium silicates phase D and phase E. Physics of the Earth and Planetary Interiors, 175, 106-114.

Sinogeikin, S. V., Bass, J. D., and Katsura, T. (2003) Single-crystal elasticity of ringwoodite to high pressures and high temperatures: implications for 520 km seismic discontinuity. Physics of the Earth and Planetary Interiors, 136, 41-66.

Sinogeikin, S. V., Zhang, J., and Bass, J. D. (2004) Elasticity of single-crystal and polycrystalline $MgSiO_3$ perovskite by Brillouin spectroscopy. Geophysical Research Letters, 31, L06620.

Stackhouse, S., Coveney, P. V., and Benoit, D. M. (2004) Density functional theory based study of the dehydroxylation behavior of aluminous dioctahedral

2:1 layer type clay minerals. Journal of Physical Chemistry B, 108, 9685-9694.

Stixrude, L. (2002) Talc under tension and compression: spinodal instability and structure at high pressure. Journal of Geophysical Research, 107, B12, 2327.

Stixrude, L., and Lithgow-Bertelloni, C. (2005) Thermodynamics of mantle minerals- I. Physical properties. Geophysical Journal International, 162, 610-632.

Syracuse, E. M., van Keken, P. E., and Abers, G. A. (2010) The global range of subduction zone thermal models. Physics of the Earth and Planetary Interiors, 183, 73-90.

Tsuchiya, J. (2013) A first-principles calculation of the elastic and vibrational anomalies of lizardite under pressure. American Mineralogist, 98, 2046-2052.

Tsuchiya, J., Tsuchiya, T., Tsuneyuki, S., and Yamanaka, T. (2002) First principles calculation of a high-pressure hydrous phase, δ-AlOOH. Geophysical Research Letters, 29, 1909.

Tsuchiya, J., Tsuchiya, T., and Tsuneyuki, S. (2005) First-principles study of hydrogen bond symmetrization of phase D under high pressure. American Mineralogist, 90, 44-49.

Tsuchiya, J., Tsuchiya, T., and Wentzcovitch, R. M. (2008) Vibrational properties of δ-AlOOH under pressure. American Mineralogist, 93, 477-482.

Tsuchiya, J., and Tsuchiya, T. (2009) Elastic properties of δ-AlOOH under pressure-first principle investigation, Physics of the Earth and Planetary Interiors, 174, 122-127.

Ulmer, P., and Trommsdorff, V. (1995) Serpentine stability to mantle depths and subduction-related magmatism. Science, 268, 858-861.

van Keken P., Hacker, B., Syracuse, E. M., Abers, G. A. (2011) Subduction factory 4:Depth-dependent flux of H_2O from subducting slabs worldwide. Journal of Geophysical Research, 116, B01401.

Walker, A. M., Hermann, J., Berry, A. J., O'Neill, H. St. C. (2007) Three water sites in upper mantle olivine and the role of titanium in the water weakening mechanism. Journal of Geophysical Research, 112, B05211.

Wang, F., Tange, Y., Irifune, T., Funakoshi, K.-i. (2012) P-V-T equation of state of stishovite up to mid-lower mantle conditions. Journal of Geophysical Research, 117, B06209.

Weaver, J. S. (1976) Application of finite strain theory to non-cubic crystals. Journal of Physics and Chemistry of Solids, 37, 711–718.

Welch, M. D., and Wunder, B. (2012) A single-crystal X-ray diffraction study of the 3.65 Å phase $MgSi(OH)_6$, a high-pressure hydroxide perovskite. Physics and Chemistry of Minerals, 39, 693-697.

Wentzcovitch, R., and Stixrude, L. (2010) Theoretical and computational methods in mineral physics: Geophysical applications. Reviews of Mineralogy and Geochemistry, 71, 483.

Williams, Q., and Revenaugh, J. (2005) Ancient subduction, mantle eclogite, and the 300 km seismic discontinuity. Geology, 33, 1–4.

Woodland, A. B. (1998) The orthorhombic to high-P monoclinic phase transition in Mg-Fe pyroxenes: can it produce a seismic discontinuity? Geophysics Research Letters, 25, 1241–1244.

Wunder, B., and Schreyer, W. (1992) Metastability of 10 Å phase in the system MgO-SiO_2-H_2O (MSH): what about MSH phases in subduction zones? Journal of Petrology, 33, 877-889.

Wunder, B., and Schreyer, W. (1997) Antigorite: high-pressure stability in the system MgO-SiO_2-H_2O (MSH). Lithos, 41, 213-227.

Wunder, B., (1998). Equilibrium experiments in the system MgO-SiO_2-H_2O (MSH): stability fields of clinohumite-OH [$Mg_9Si_4O_{16}(OH)_2$], chondrodite-OH [$Mg_5Si_2O_8(OH)_2$] and phase A [$Mg_7Si_2O_8(OH)_6$]. Contribution to Mineralogy and Petrology, 132, 111-120.

Wunder, B., Wirth, R., and Koch-Müller, M. (2011) The 3.65 Å phase in the system MgO-SiO_2-H_2O: Synthesis, composition, and structure. American Mineralogist, 96, 1207-1214.

Wunder, B., Jahn, S., Koch-Müller, M., and Speziale, S. (2012) The 3.65 Å phase, $MgSi(OH)_6$: structural insights from DFT-calculations and T-dependent IR spectroscopy. American Mineralogist, 97, 1043-1048.

Yang, H., Prewitt, C. T., and Frost, D. J. (1997) Crystal structure of the dense hydrous magnesium silicate, phase D. American Mineralogist, 82, 651–654.

Yeganeh-Haeri, A., Weidner, D. J., and Ito, E. (1989) Elasticity of $MgSiO_3$ in the perovskite structure. Science, 243, 787-789.

Zha, C.-S., Mao, H.-k., and Hemley, R. (2000) Elasticity of MgO and a primary pressure scale to 55 GPa. Proceedings of National Academy of Sciences of the United States of America, 97, 13494–13499.

Figure Captions

Figure 1. (a) Ternary diagram in (mol %) modified from (Wunder et al., 2012) showing various hydrous phases in the MgO-SiO_2-H_2O (MSH) system, including 3.65 Å phase. Mineral abbreviations and stoichiometry: ant- antigorite ($Mg_{2.8}Si_2O_5(OH)_4$), br- brucite ($Mg(OH)_2$), tlc- talc ($Mg_3Si_4O_{10}(OH)_2$); 10 Å - 10 Å phase ($Mg_3Si_4O_{10}(OH)_2.H_2O$), 3.65 Å- 3.65 Å phase ($MgSi(OH)_6$), clinohum- clinohumite ($Mg_9Si_4O_{16}(OH)_2$), chond- chondrodite ($Mg_5Si_2O_8(OH)_2$), phA- phase A ($Mg_7Si_2O_8(OH)_6$), phB- phase B ($Mg_{12}Si_4O_{19}(OH)_2$), ShyB- superhydrous phase B ($Mg_{10}Si_3O_{10}(OH)_4$), phD- phase D ($MgSi_2H_2O_6$), phE- phase E ($Mg_{2.23}Si_{1.81}H_{2.8}O_6$), cen- clino enstatite ($MgSiO_3$), mj- majorite ($MgSiO_3$), pv- bridgmanite/perovskite ($MgSiO_3$), ol- olivine (Mg_2SiO_4), wad-wadsleyite (β-Mg_2SiO_4), ri- ringwoodite (γ-Mg_2SiO_4). (b-d) Crystal structure of the 3.65 Å phase from *first principles* simulations corresponding to the unit-cell volume of 200 $Å^3$. There are several O-H---O units that loosely form a "crankshaft" pattern that run parallel to the z-direction. This is highlighted by a dashed line and is evident when the crystal structure is viewed down the y-axis and x-axis. These patterns become prominent as the symmetrization of hydrogen bond occurs. The O-H and H---O bond lengths become equal. Note that the O(1)-H(1)---O(1) and O(2)-H(2)---O(2) do not exhibit symmetrization. The crystal structure is viewed down the y-axis, x-axis and z- axis in the (b), (c), and (d) respectively.

Figure 2. X-ray diffraction pattern, plotted after background subtraction, of the 3.65 Å phase at ambient pressure (in the diamond anvil cell), 9.9 GPa,

873 19.3 GPa, 30.4 GPa, 41.0 GPa and in decompression at 25.2 GPa, 8.0 GPa
874 and 0.1 GPa. In the ambient pressure spectrum the black open circles
875 represent the collected data and the black line denotes the Le Bail
876 refinement. The black crosses denote the presence of amounts up to 10 %
877 of 10 Å phase. The black asterisks indicate Ne peacks. The vertical red and
878 black tick marks denote the peak positions corresponding to the 3.65 Å
879 phase and the 10 Å phase calculated at ambient conditions. The most
880 intense diffraction peaks of the 3.65 Å phase are labeled in the pattern
881 collected at 0.1 GPa in decompression (at the top of the figure). Note in all
882 the patterns the intense peak at 3.65 Å that is characteristic of the phase.
883
884 **Figure 3.** Equation of state and linear compressibility of the 3.65 Å phase from
885 experiment and *first principles* simulations -(**a**) plot of pressure vs. unit-
886 cell volume; (**b**) plot of lattice parameters *a*, *b*, and *c* vs. unit-cell volume;
887 (**c**) plot of lattice parameter b vs. unit cell volume. The green shaded area
888 represents a 2^0 interval within which the experimental data lies. The *first*
889 *principles* simulation results shows very little deviation from $\sim 90^0$
890 indicating only a slight distortion from the orthorhombic symmetry; (**d**)
891 finite strain (f_V) vs normalized pressure (F_V) plot. The third-order and
892 fourth order finite strain fits are represented by dashed green line and
893 green line respectively. (**e**) linear normalized pressure (f_l) vs linear
894 normalized pressure (F_l) for the lattice parameter *a*, *b*, and *c*.
895
896 **Figure 4.** Full elastic constant tensor vs. pressure- (**a**) three principal elastic
897 constants, (**b**) six off diagonal elastic constants, and (**c**) four shear elastic

898 constants, (**d**) bulk and shear modulus vs. pressure. The Voigt and Reuss
899 limits are indistinguishable for the bulk modulus at all pressures. For the
900 shear modulus, the two limits diverge out at high pressure; (**e**) elastic
901 anisotropy as a function of pressure; (**f**) aggregate compressional (V_P) and
902 shear (V_S) wave velocity at static condition as function of pressure. Also
903 shown is the (V_P/V_S) ratio as a function of pressure.
904
905 **Figure 5.** Behavior of proton under compression - (a) O-H (hydroxyl) and O---H
906 (hydrogen) bond lengths as a function of density/pressure; (b) plot of O-
907 H bond distance as a function of O---O distances, the "black line"
908 represents the condition for symmetric hydrogen bonding i.e., O-H bond
909 distance = half of O---O distance; (c) the angle between the O-H vector and
910 the O----O vector. An angle of 180° indicates strong hydrogen bonding and
911 as in the case of O(5)-H(4)---O(4) and O(6)-H(3)---O(3) at high pressures;
912 (e) plot of MgO_6 and SiO_6 relative compression octahedral volume as a
913 function of pressure indicate that MgO_6 is more compressible than the
914 SiO_6 units. Inset shows the plot of Mg-Si-O angle as a function of pressure.
915
916 **Figure 6.** Bulk moduli and density systematics for various hydrous mineral
917 phases in MSH ternary system. Bulk moduli and density data for the
918 mineral phases are colored based on their water content. The dark
919 symbols represent lower or no water content whereas lighter symbols
920 represent water rich phases. Please see the vertical color scale in the right.
921 The color scale helps to distinguish the dry, nominally anhydrous, and
922 hydrous phases. The symbol sizes are also proportional to water content.

Hence the darker symbols are smaller in size, and lighter symbols are larger in size. The abbreviations for the minerals are same as in Fig. 1a. Inset shows the plot of bulk sound velocity along the $MgSiO_3$-H_2O join with bridgmanite, majorite, clinoenstatite, 3.65 Å phase, and H_2O. All data are from literature, reported in **Table 4**.

Figure 7. Maximum compressional (AV_P) and shear (AV_S) elastic anisotropy for LHMS and DHMS phases as a function of pressure. Mineral abbreviations-ant refers to antigorite, ShyB refers to superhydrous phase B. Elastic anisotropy data for LHMS and DHMS are from, B13- Bezacier et al., (2013); M08- Mainprice et al., 2008; S08- Sanchez-Valle et al., (2008); M07- Mainprice et al., (2007); R12- Rosa et al., (2012); PW96- Pacalo and Weidner (1996). The X-discontinuity and the mantle transition zone are denoted by the orange and the grey band, respectively. Also shown are the stability fields of antigorite, ~ 7 GPa (Liu, 1986; Ulmer and Trommsdorff, 1995), 10 Å phase ~9 GPa (Pawley and Wood, 1995; Pawley et al., 2011) and the formation of the 3.65 Å phase at 9 GPa. The 3.65 Å phase is likely to decompose to HPCen and water beyond 500 ^oC (Wunder et al., 2011).

Table 1. Details of experimental conditions explored in this study

Exp #	λ (Å)	E (keV)	P_{min} (GPa)	P_{max} (GPa)	Pressure Callibrant	Pressure generation method
I[a]	0.2897	42.80	$1e^{-05}$	41.00	Ruby, Au	gas-membrane
II[b]	0.2904	42.70	6.20	26.30	Ruby	gas-membrane
III[b]	0.2922	42.43	1.00	5.90	Ruby[c]	manual

[a] data were collected for both compression and de-compression paths; [b] data were collected only for compression path; [c] pressure was measured offline.

Table 2. Finite strain fit parameters for bulk and linear compressibility.

	V_0 (Å^3)	K_0 (G Pa)	K'	K''
	Experiments (*this study*)			
4th	194.52* (0.02)	77 (2)	7.9 (0.8)	-0.7 (0.2)
3rd	194.52 (0.02)	83 (1)	4.9 (0.2)	
	First principles simulation (this study)			
4th	202.02	80	3.4	-0.05
	Experiments (*this study*)			
	l_0 (Å)	K_l (G Pa)	m_l	
a	5.1131 (0.0003)	208.6 (1.1)	685.9 (18.8)	
b	5.1898 (0.0003)	293.3 (1.2)	-66.8 (20.9)	
c	7.3303 (0.0004)	282.3 (1.4)	767.6 (27.6)	
β	90.03^o (0.01)			
	First principles simulation (*this study*)			
a	5.170	224.8 (1.5)	-77.5 (13.3)	
b	5.267	241.6 (7.4)	-125.7 (7.4)	
c	7.420	261.1 (9.9)	201.2 (115)	
β	89.69^o			

*The experimental V_0 were measured in GFZ [*Wunder et al.,* 2012]

Table 3 Full elastic constant tensor (C_{ij}), bulk (K), and shear (G) modulus for 3.65 Å phase as a function of pressure, volume, and density.

P	V	ρ	C_{11}	C_{22}	C_{33}	C_{44}	C_{55}	C_{66}	C_{46}	C_{12}	C_{13}	C_{23}	C_{15}	C_{25}	C_{35}	K_V	K_H	K_R	G_V	G_H	G_R
[GPa]	[Å^3]	[g/cm^3]	[GPa]																		
-5.9	220	2.33	126.5	128.4	131.1	46.1	50.9	53.4	-2.3	20.2	22.4	17.3	-0.8	-0.7	1.7	56.2	56.2	56.2	51.8	51.7	51.5
-2.9	210	2.44	134.9	148.0	156.7	52.7	53.0	64.1	-0.3	27.4	18.6	18.5	0.6	0.6	-0.2	63.2	63.1	63.1	59.0	58.6	58.3
0.8	200	2.56	162.9	173.8	194.1	54.9	59.8	77.4	1.9	40.8	29.5	24.0	2.2	2.7	-2.1	79.9	79.9	79.8	67.5	66.7	65.9
5.4	190	2.70	197.5	206.8	241.3	60.6	67.3	92.7	4.7	55.4	37.2	30.7	3.9	3.6	-4.9	99.1	99.0	99.0	79.0	77.4	75.8
11.2	180	2.85	246.9	264.4	316.3	70.3	78.3	110.3	8.5	82.0	60.1	49.2	5.0	4.3	-9.1	134.5	134.3	134.1	94.2	91.7	89.3
18.5	170	3.02	286.8	298.7	388.0	75.5	89.8	130.1	12.3	102.3	77.6	64.9	7.4	6.4	-13.4	162.6	162.0	161.5	107.7	103.9	100.1
27.6	160	3.21	358.3	371.3	477.6	82.0	105.3	151.1	16.2	140.3	105.2	95.2	9.5	7.9	-18.4	209.8	209.3	208.7	125.4	120.1	114.8
39.1	150[1]	3.42	449.6	458.4	600.4	86.5	130.6	172.9	22.1	190.3	154.3	142.4	13.4	9.1	-25.8	275.8	274.9	273.9	146.1	138.5	130.8
53.8	140	3.66	568.2	636.0	801.2	95.3	153.7	195.5	25.8	273.1	229.3	241.7	21.0	7.7	-35.6	388.2	385.7	383.2	173.0	162.2	151.5
72.6	130	3.94	705.2	771.0	950.7	83.0	170.2	231.0	33.1	367.8	308.3	328.2	26.1	13.4	-41.5	492.8	490.5	488.2	191.7	173.0	154.2
97.0	120	4.27	881.8	964.1	1138.8	59.1	189.9	275.5	41.8	499.0	418.0	444.7	31.8	23.2	-48.2	634.3	632.1	629.9	213.1	175.4	137.7
finite strain fit																					
0.0	202	2.54	156.2	169.4	189.3	55.9	58.5	74.8	1.6	38.0	26.5	22.9	1.5	1.5	-1.9	76.2	76.1	76.1	66.0	65.1	64.4
			7.2	7.3	11.1	1.5	1.7	3.2	0.6	3.2	2.7	1.6	0.3	0.3	-0.6	4.8	4.9	4.8	2.4	2.3	2.1

[1]elasticity data up to volume of 150 Å^3 were used to constrain the finite strain fit parameters.

Table 4. Density and bulk moduli for various hydrous mineral phases in the MSH ternary.

Mineral Phase	Formula	ρ_0 [gm cm^{-3}]	K_0 [GPa]	H_2O [wt%]	Reference
		MgO-SiO_2-H_2O end members			
Periclase	MgO	3.585	160.2	0.00	Zha et al., (2000)
Stishovite	SiO_2	4.287	294.0	0.00	Wang et al., (2012)
Ice-III	H_2O	1.159	9.3	100.00	Tulk et al., (1994)
Liquid water	H_2O	0.997	2.2	100.00	Kell et al., (1975)
		Normal mantle phases and nominally anhydrous mineral phases			
Olivine	Mg_2SiO_4	3.218	125.5	0.00	Downs et al., (1996)
Clinoenstatite	$MgSiO_3$	3.301	118.3	0.00	Kungetal., (2005); Jackson et al., (2010)
Majorite	$MgSiO_3$	3.522	159.8	0.00	Pacalo and Weidner, (1997)
Bridgemanite	$MgSiO_3$	4.098	256.7	0.00	Yagi et al., (1978); Tange et al., (2012)
Hydrous olivine	Mg_2SiO_4	3.180	125.4	0.90	Mao et al., (2010)
Hydrous wadsleyite	β-Mg_2SiO_4	3.435	161.3	0.84	Mao et al., (2008)
Hydrous ringwoodite	γ-Mg_2SiO_4	3.649	175.2	1.10	Mao et al., (2012)
		Layered hydrous magnesium silicates (LHMS)			
Brucite	$Mg(OH)_2$	2.380	43.8	30.89	Jiang et al., (2006)
Serpentine	$Mg_3Si_2O_5(OH)_4$	2.620	68.5	13.00	Bezacier et al., (2013)
Talc	$Mg_3Si_4O_{10}(OH)_2$	2.750	41.0	4.75	Pawley et al., (2002)
10 Å phase	$Mg_3Si_4O_{10}(OH)_2.H_2O$	2.676	39.0	9.50	Comodi et al., (2006)
		Dense hydrous magnesium silicates (DHMS)			
3.65 Å phase	$MgSi(OH)_6$	2.636	84.0	35.00	***this study***
clinohumite	$Mg_9Si_4O_{16}(OH)_2$	3.187	119.4	2.90	Ross and Crichton, (2001)
chondrodrite	$Mg_5Si_2O_8(OH)_2$	3.057	115.7	5.30	Ross and Crichton, (2001)
phase A	$Mg_7Si_2O_8(OH)_6$	2.976	106.0	11.84	Sanchez-Valle et al., (2006)
phase B	$Mg_{12}Si_4O_{19}(OH)_2$	3.368	163.0	2.43	Finger et al., (1989); Kudoh et al., (1995)
superhydrous phase B	$Mg_{10}Si_3O_{10}(OH)_4$	3.327	154.0	6.49	Pacalo and Weidner, (1996)
phase D	$MgSi_2H_2O_6$	3.459	166.0	18.49	Frost and Fei, (1999)
phase E	$Mg_{2.23}Si_{1.81}H_{2.8}O_6$	2.920	93.0	13.60	Shieh et al., (2000)

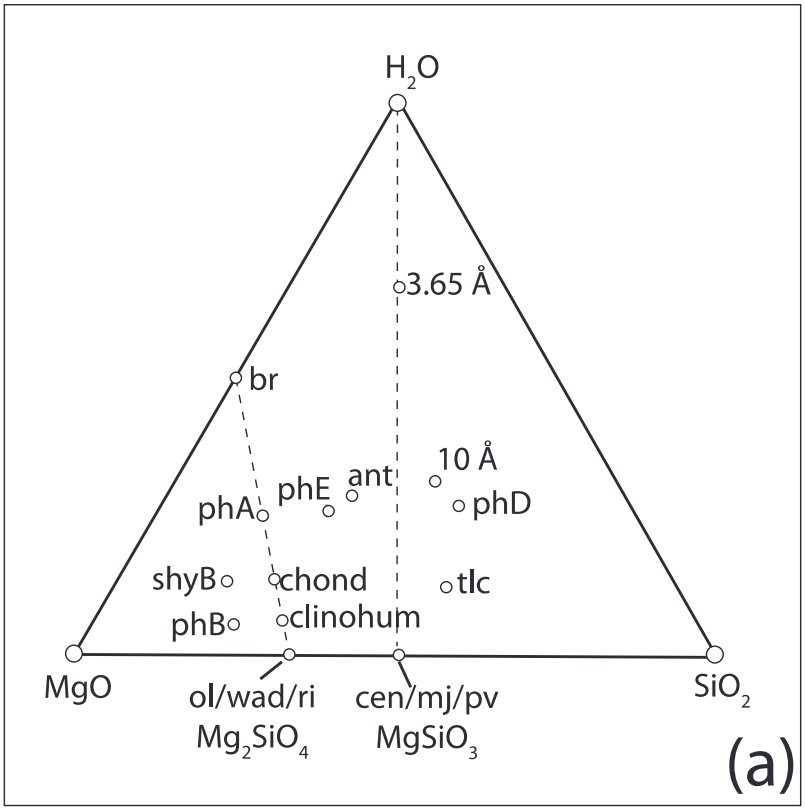
H2O
3.65 Å
br
10 Å
ant
phE
phA
phD
shyB
chond
tlc
phB
clinohum
MgO
ol/wad/ri
Mg2SiO4
cen/mj/pv
MgSiO3
SiO2
(a)

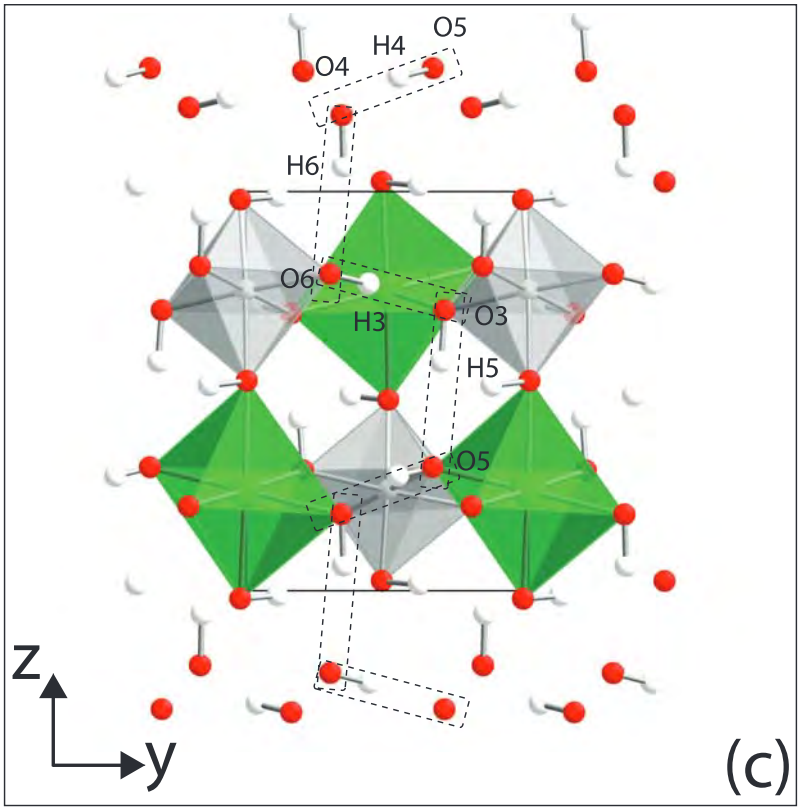
O5
H4
O4
H6
O6
H3
O3
H5
O5
z
y
(c)

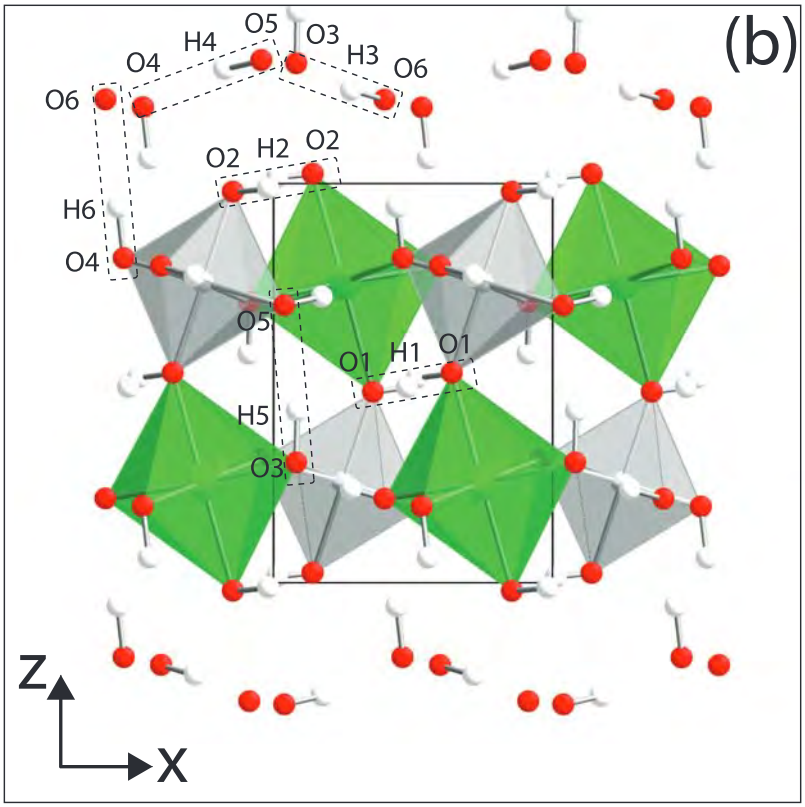
(b)
O5
H4
O3
O4
H3
O6
O6
O2
H2
O2
H6
O4
O5
O1
H1
O1
H5
O3
z
x

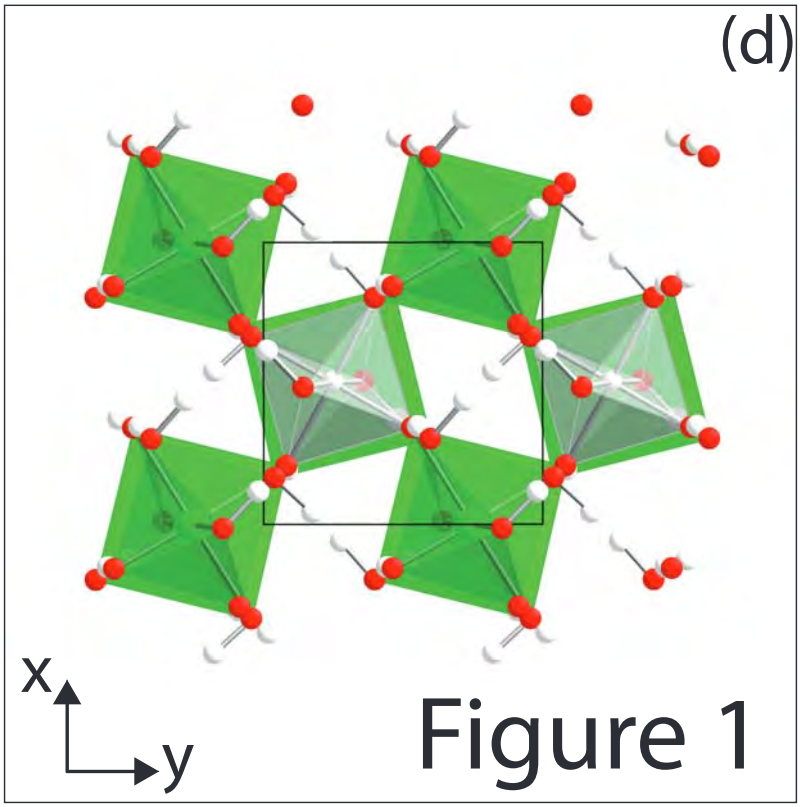
(d)
x
y

Figure 1

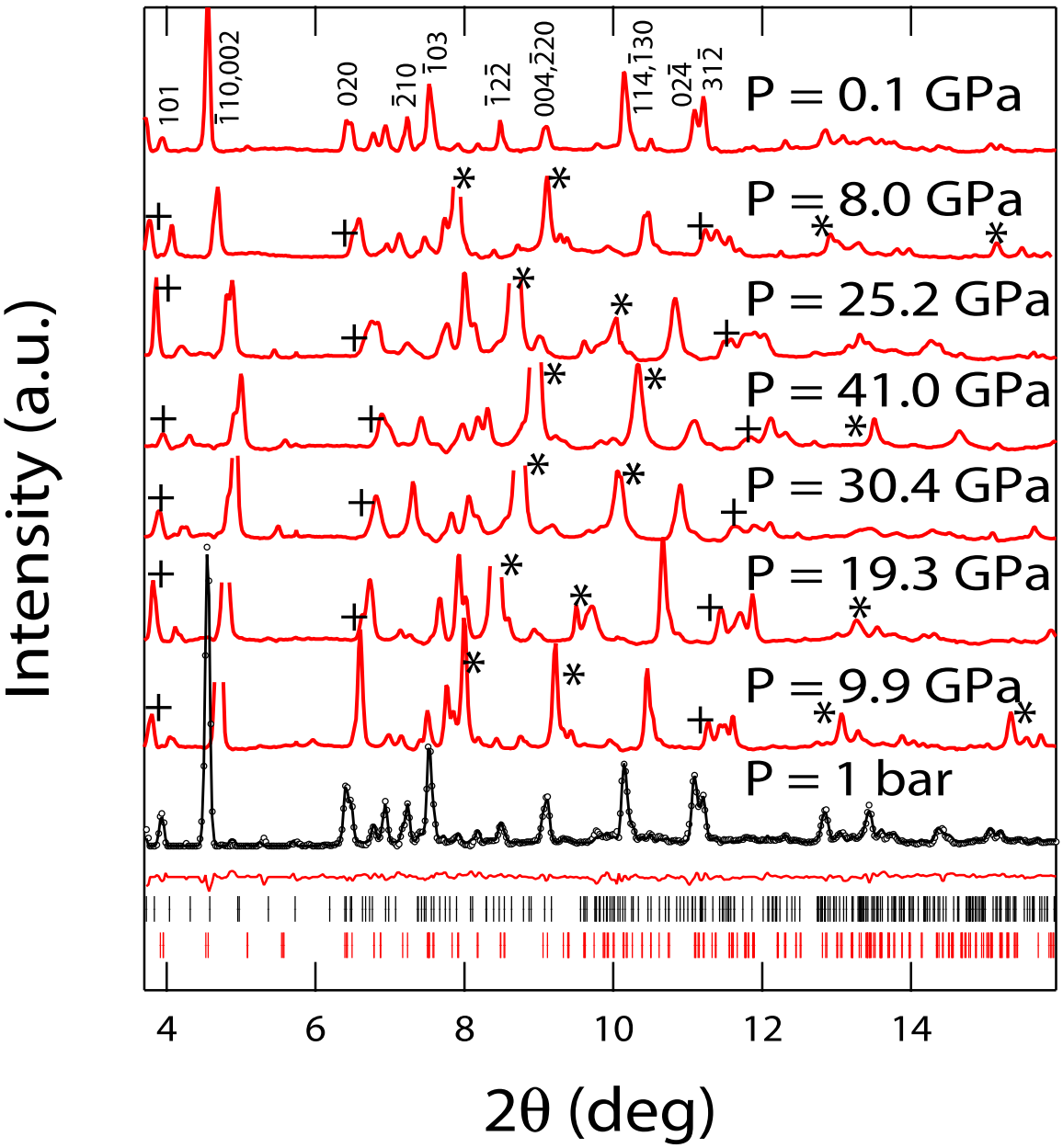
Intensity (a.u.)
101
$\bar{1}$10,002
020
$\bar{2}$10
$\bar{1}$03
$\bar{1}$22
004,$\bar{2}$20
114,$\bar{1}$30
02$\bar{4}$
31$\bar{2}$
P = 0.1 GPa
P = 8.0 GPa
P = 25.2 GPa
P = 41.0 GPa
P = 30.4 GPa
P = 19.3 GPa
P = 9.9 GPa
P = 1 bar
4
6
8
10
12
14
2θ (deg)

Figure 2

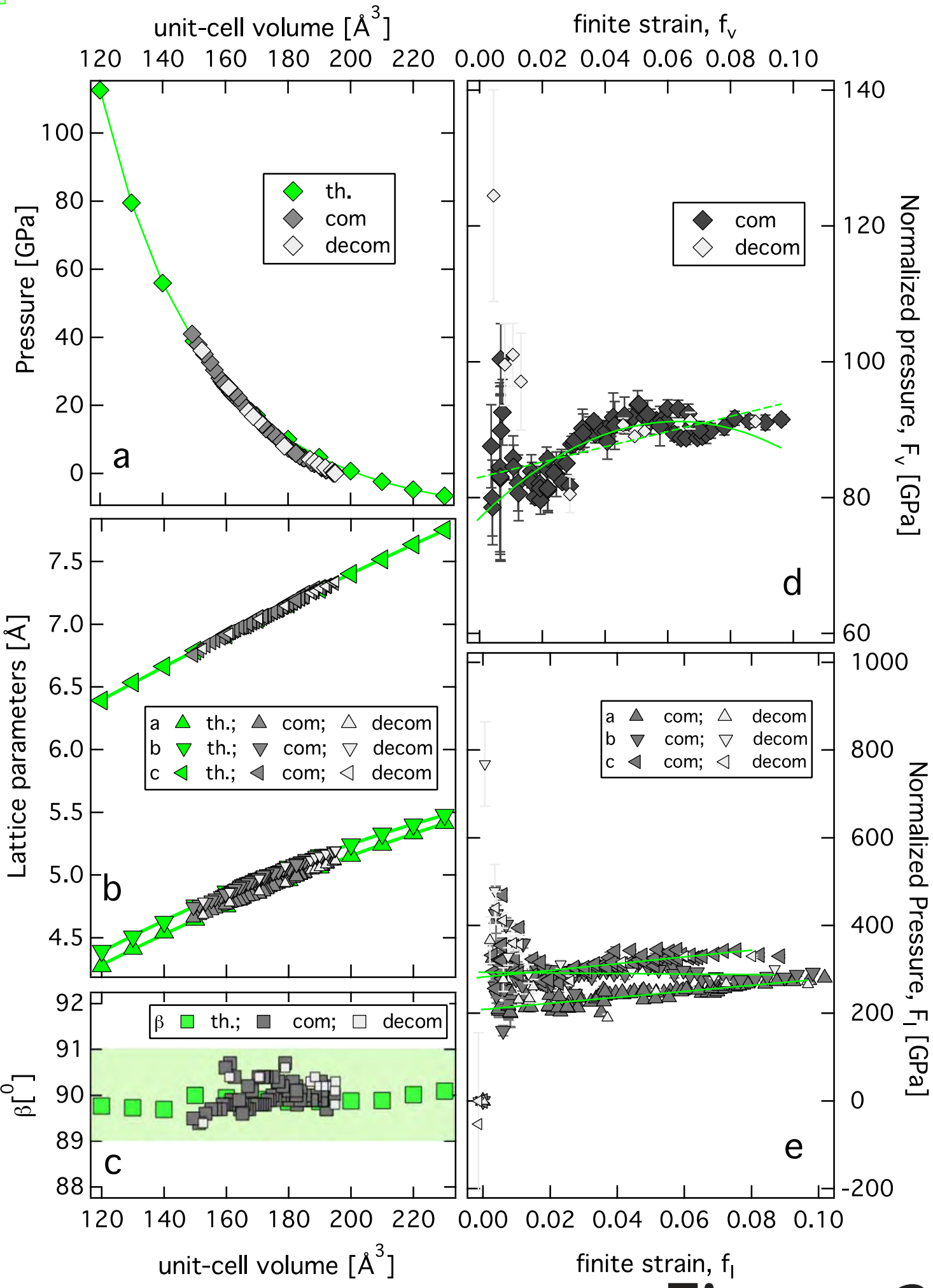
unit-cell volume [Å^3]
finite strain, f_v
Pressure [GPa]
Normalized pressure, F_v [GPa]
Lattice parameters [Å]
Normalized Pressure, F_f [GPa]
β[^{0}]
unit-cell volume [Å^3]
finite strain, f_f
th.
com
decom
a
b
c
d
e
a th.; com; decom
b th.; com; decom
c th.; com; decom
a com; decom
b com; decom
c com; decom
β th.; com; decom

Figure 3

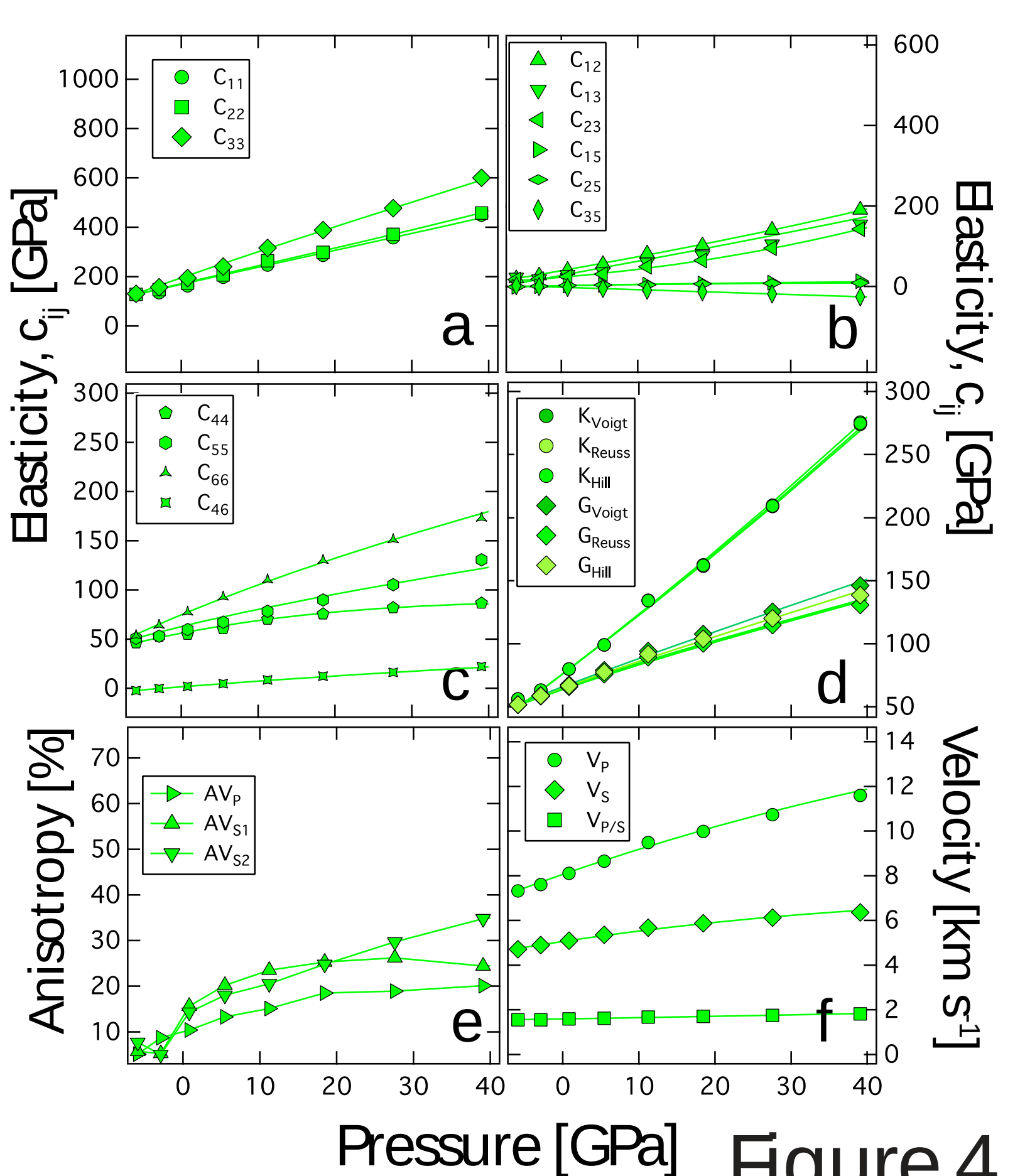
Elasticity, c_{ij} [GPa]
C_{11}
C_{22}
C_{33}
a
C_{12}
C_{13}
C_{23}
C_{15}
C_{25}
C_{35}
b
Elasticity, c_{ij} [GPa]
C_{44}
C_{55}
C_{66}
C_{46}
c
K_{Voigt}
K_{Reuss}
K_{Hill}
G_{Voigt}
G_{Reuss}
G_{Hill}
d
Anisotropy [%]
AV_P
AV_{S1}
AV_{S2}
e
V_P
V_S
$V_{P/S}$
f
Velocity [km s^{-1}]
Pressure [GPa]

Figure 4

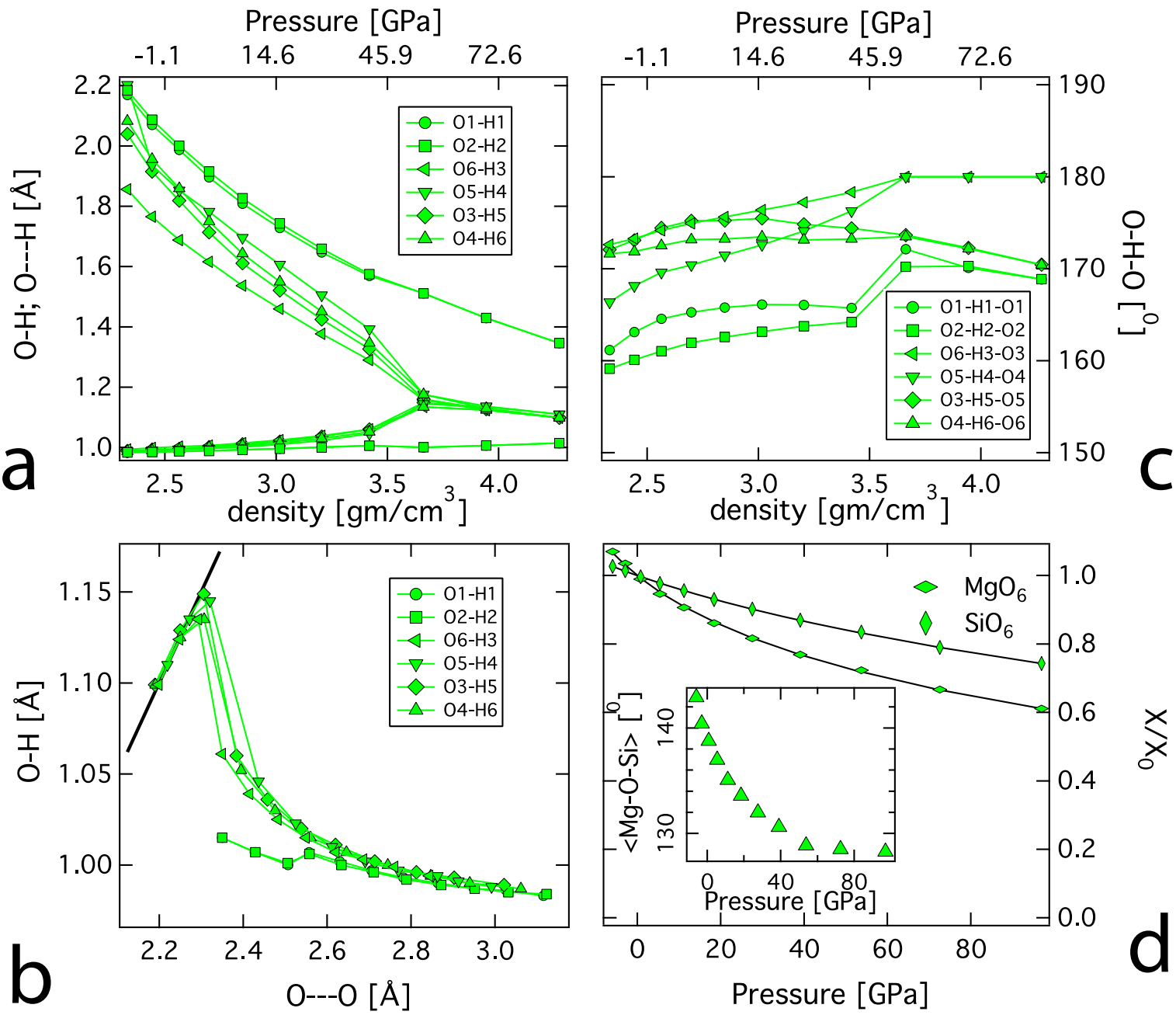
Pressure [GPa]
-1.1
14.6
45.9
72.6
O-H; O--H [Å]
density [gm/cm3]
O1-H1
O2-H2
O6-H3
O5-H4
O3-H5
O4-H6
a
O-H-O [°]
O1-H1-O1
O2-H2-O2
O6-H3-O3
O5-H4-O4
O3-H5-O5
O4-H6-O6
c
O-H [Å]
O---O [Å]
b
MgO6
SiO6
<Mg-O-Si> [°]
X/X0
Pressure [GPa]
d

Figure 5

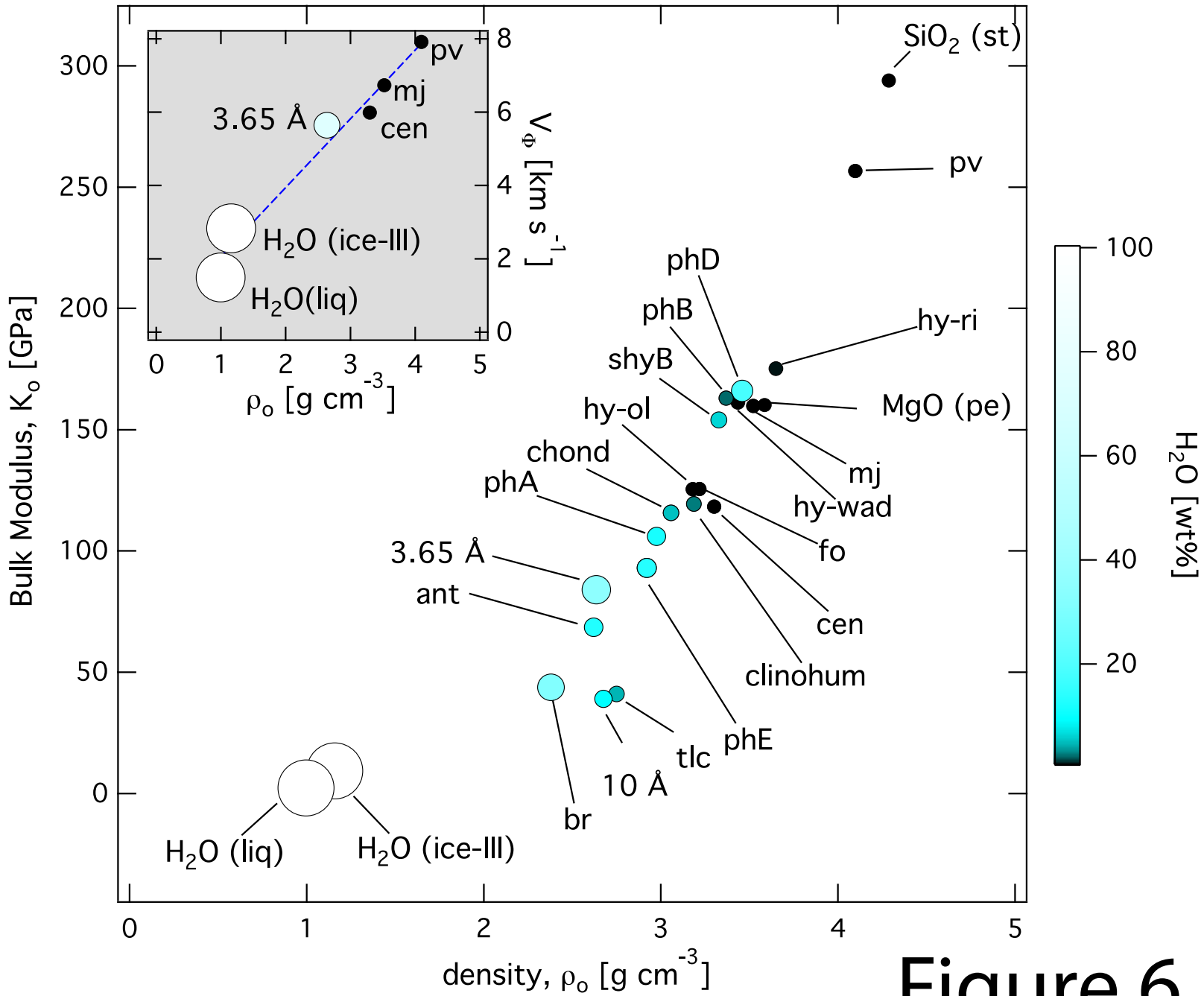
SiO2 (st)
pv
phD
phB
hy-ri
shyB
MgO (pe)
hy-ol
chond
mj
phA
hy-wad
fo
3.65 Å
ant
cen
clinohum
phE
tlc
10 Å
br
H2O (liq)
H2O (ice-III)
Bulk Modulus, Ko [GPa]
density, ρo [g cm-3]
H2O [wt%]
pv
mj
cen
3.65 Å
H2O (ice-III)
H2O(liq)
ρo [g cm-3]
VΦ [km s-1]

Figure 6

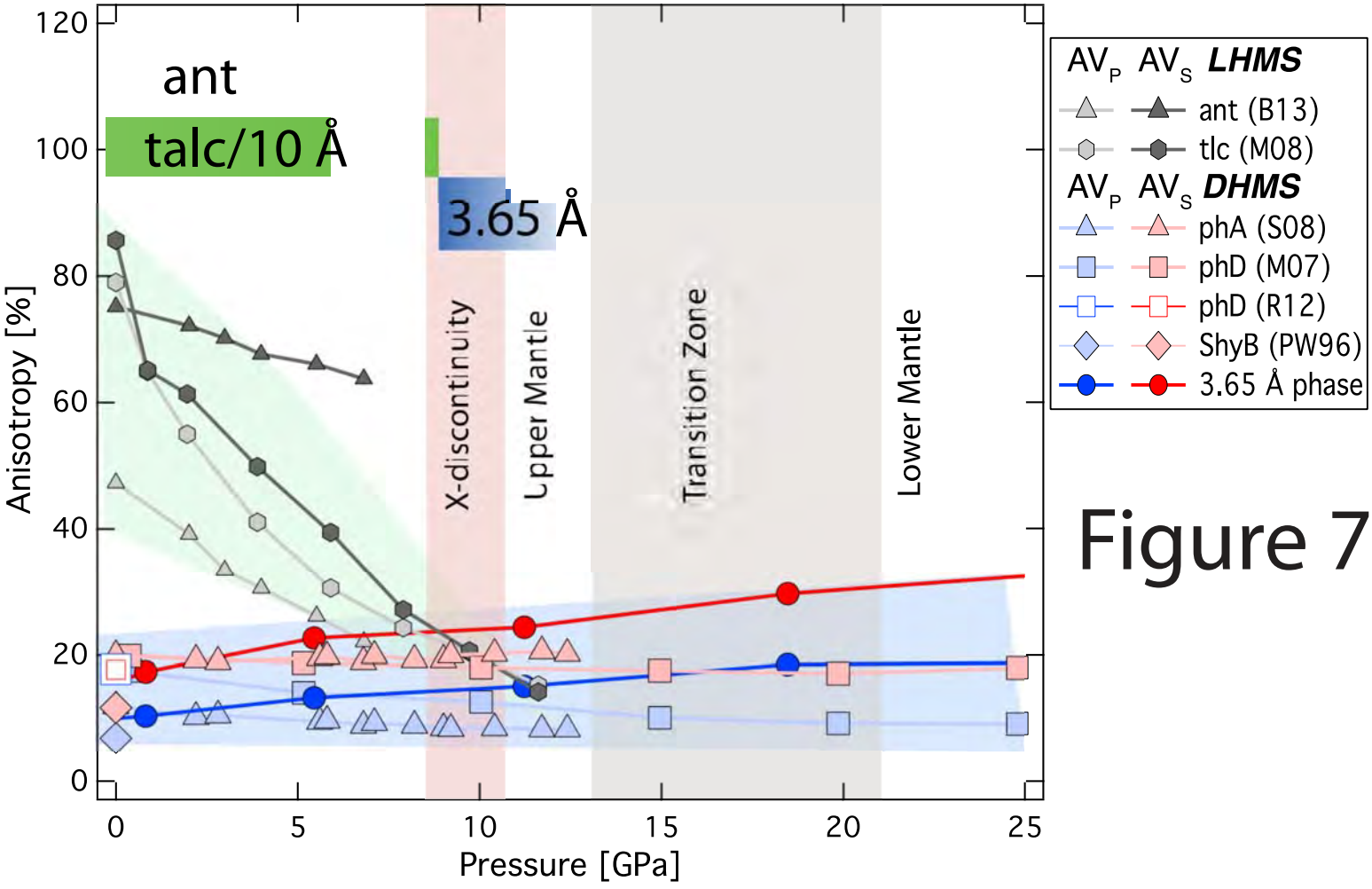
ant
talc/10 Å
3.65 Å
X-discontinuity
Upper Mantle
Transition Zone
Lower Mantle
Anisotropy [%]
Pressure [GPa]
0
20
40
60
80
100
120
0
5
10
15
20
25
AVP AVS LHMS
ant (B13)
tlc (M08)
AVP AVS DHMS
phA (S08)
phD (M07)
phD (R12)
ShyB (PW96)
3.65 Å phase

Figure 7